

Contents lists available at [ScienceDirect](https://www.sciencedirect.com)

International Journal of Machine Tools and Manufacture

journal homepage: www.elsevier.com/locate/ijmactool

Towards understanding the thermal history of microstructural surface deformation when cutting a next generation powder metallurgy nickel-base superalloy

Andrea la Monaca^a, Dragos A. Axinte^{a,*}, Zhirong Liao^a, Rachid M'Saoubi^b, Mark C. Hardy^c

^a Rolls-Royce UTC in Manufacturing and On-Wing Technology, University of Nottingham, Nottingham, NG8 1BB, United Kingdom

^b R&D Material and Technology Development, Seco Tools AB, 737 82, Fagersta, Sweden

^c Rolls-Royce plc, PO Box 31, Derby, DE24 8BJ, United Kingdom

ARTICLE INFO

Keywords:

Surface integrity
Nickel-base superalloy
Cutting temperature
Machining
White layer
Material drag

ABSTRACT

Despite the ongoing progress in metallurgical characterisation of machined surfaces, knowledge of the thermal conditions under which they originate during the workpiece-flank interaction is still lacking. When cutting advanced superalloys, little is known about temperature evolution in the machined part volume, where workpiece material interacts with the tool flank. In this work, the characteristics of the thermal field and the resulting surface metallurgy induced in a next generation nickel-base superalloy have been studied for cutting scenarios involving different combinations of thermo-mechanical boundary conditions. Analysis of the thermal field evolution in the workpiece subsurface has allowed the heating and cooling rates induced by cutting to be revealed, allowing description of two distinct types of thermal cycle, with a Heating-Peaking-Cooling (H-P-C) and a Heating-Quasi-isothermal Deformation-Cooling (HQC) structure depending on the process aggressiveness. Subsurface thermal history has been found to relate with the severity of the cutting-induced deformation, as it combines information on thermal field magnitude and on the process rates. Furthermore, thermal balance equations have been applied to study the rate of the heat generation in the machined subsurface due to its own plastic deformation while interacting with the tool flank. This has revealed that the highest rate of heat generation induced by plastic deformation occurred in thin surface layers at the beginning of the workpiece-flank contact, which has been associated to the conditions under which white layers (WLs) are generated. Energy balance analysis has furthermore indicated the development of a less severe and less impulsive deformation process at higher subsurface depths, which has been linked to the formation mechanism of material drag (MD) layers. In this way, the thermal history of machined surfaces has been related to their resulting metallurgical integrity, allowing in-depth understanding of the physical conditions developing when cutting next-generation superalloys.

1. Introduction

Understanding the mechanisms of microstructural modification induced by machining processes to high performance alloys represents a fundamental research topic with high relevance from both an academic and industrial perspective. In fact, significant research interest is attracted by the mechanisms governing the instantaneous microstructural alteration that can be induced in a machined surface during its interaction with a cutting insert [1]. Moreover, as the machining-induced surface integrity can play a crucial role in determining a material's ability to withstand in-service loading conditions, its

understanding is particularly relevant from an industrial perspective within the manufacture of high value components in fields such as aerospace, nuclear or automotive [2].

Although research attention has been focused in the past on the role of thermal and mechanical effects on the formation of machining-induced surface anomalies [1], the following literature analysis will argue that, despite its primary role to describe the mechanisms of microstructural deformation in machining, the study of the thermal history of machined surfaces represents a topic significantly unexplored.

During chip formation, intensive material deformation simultaneously occurs in three distinct regions adjacent to the tool workpiece

* Corresponding author.

E-mail address: Dragos.Axinte@nottingham.ac.uk (D.A. Axinte).

<https://doi.org/10.1016/j.ijmactools.2021.103765>

Received 4 October 2020; Received in revised form 29 May 2021; Accepted 12 June 2021

Available online 19 June 2021

0890-6955/© 2021 The Authors. Published by Elsevier Ltd. This is an open access article under the CC BY license (<http://creativecommons.org/licenses/by/4.0/>).

interface, where high temperature and strain locally develop at extreme rates [3]. These are: (i) primary shear zone (PSZ), constituted by fast shearing metal volumes transitioning from the workpiece material to the forming chip; (ii) secondary shear zone (SSZ), developing by friction at the tool-chip contact region; (iii) tertiary shear zone (TSZ), where plastic deformation occurs due to the interference of the workpiece new (machined) surface with the tool flank.

Because of their predominant contribution to heat generation in cutting, the temperature fields developing in PSZ and SSZ have been object of numerous investigations over the past years, with state-of-the-art research being currently focused on the investigation of heat transfer phenomena in these two shear zones and on the determination of key parameters for their thermal analysis. However, many of the research works investigating the cutting-induced thermal field hardly give a perspective on the phenomena in TSZ, i.e. at the flank-workpiece interface. Hao et al. [4] have studied the formation of thermal contact resistance in cutting by means of high-speed thermal imaging and scanning electron microscopy (SEM), highlighting its influence on heat conduction at the tool-workpiece interface. However, the thermal conditions induced to the machined surface volume have not been analysed. Kryzhanivskyy et al. [5,6] have discussed the transient thermal field at the tool-workpiece interface, implementing an approach able to estimate the time evolution of heat flux and tool-chip thermal conductance by means of an inverse problem technique. Nevertheless, the thermal phenomena developing at the flank-workpiece interface in TSZ are not investigated. Nemetz et al. [7] have studied the cyclic thermal loading in coated milling inserts, in relation to the substrate plastic deformation. However, it is not known how this relates to the thermal fields experienced by the workpiece surface in TSZ and to the resulting component integrity.

Although there exists a number of research works investigating the machined surface temperature in cutting, a significant gap is still present, as knowledge lacks on how such surface temperature relates to the microstructural condition induced by machining. With focus on a Cu alloy, Huang et al. [8] developed an improved heat-source model aiming to represent the machined surface temperature evolution in cutting including the effect of heating and cooling rates. Nevertheless, the implications of such thermal effects on the resulting surface integrity were not investigated. Chen et al. [9] studied the temperature evolution in hard turning of hardened steels, showing how the peak temperature on the machined surface is reached at its intersection with the cutting edge, and presenting two experimental approaches for the surface temperature measurement. However, it is not known how the investigated thermal phenomena relate to the machined surface condition. Cuesta et al. [10] have applied infrared temperature measurement to evaluate the heat transferred to the workpiece when drilling Inconel 718, showing its variability in dry and wet conditions. However, the link between surface temperatures in TSZ and the resulting surface metallurgy has not been explored.

The aforementioned lack of information on the thermal field evolution in TSZ in relation to the subsurface deformation induced by machining appears to be a significant limitation and in stark contrast with the remarkable progress on the investigation of the small-scale metallurgical features of machined surfaces.

In fact, when metallurgical surface integrity is a foremost requirement to ensure part performance, the presence of machining-induced microstructural alterations needs to be thoroughly assessed [11]. M'Saoubi et al. [12] have studied the sensitivity of four nickel-base superalloys (i.e. Inconel 718, Waspaloy, Alloy 720Li and RR1000) to aggressive drilling conditions, providing an in-depth metallurgical characterisation of the nano-scale properties of machining-induced layers presenting severe plastic deformation (SPD). Although this work proposes a temperature-based interpretation of the SPD layer formation, this is based on finite element (FE) modelling to identify representative cutting temperatures. However, the thermal evolution in the workpiece subsurface during the plastic deformation process still

represents an open question. Hosseini et al. [13] have investigated the formation mechanisms of white layers (WLs) produced by hard turning in AISI 52100 steel, discussing the effect of cutting-induced processing conditions on the nano-scale recrystallization of mechanically and thermally induced WLs. However, knowledge is missing on the subsurface thermal evolution under which this microstructural deformation and recrystallization process takes place. Xu et al. [14] have proposed a method to investigate the relationship between surface integrity, cutting energy and chip formation when machining Ni-base superalloys. These energetic considerations rely on macroscopic analyses of the cutting process, i.e. through cutting forces and speed measurements. However, it would be interesting to reach a local energetic description (e.g. in the form of local heat generation) of the surface deformation process in TSZ. Brown et al. [15] quantitatively characterised WLs induced by mechanical material removal in Ti-6Al-4V, discussing the generation mechanisms of SPD in relation to this material. Also in this case, it would be interesting to relate such plastic deformation process to the thermal gradients developing in TSZ during machining. Studying the surface integrity of Inconel 718 over multiple length scales, it was discussed in Ref. [16] how the insert material, its wear state, and the material removal rate could influence the resulting surface deformation after mechanical machining. However, it is unclear how such processing conditions influenced the thermo-mechanical conditions in TSZ, which could relate to the microstructural deformation induced to the workpiece. Liao et al. [17] have furthermore revealed the grain refinement mechanism induced when cutting a novel nickel-base superalloy, where the observed nano-scale recrystallization and gamma prime dissolution process have been associated to the extreme heating and cooling rates induced by mechanical machining operations. However, an actual investigation on such heating and cooling rates is missing, as the thermal history of machined surface deformation in TSZ is still an unknown topic. Thus, despite the unprecedented knowledge being disclosed on the metallurgy of machined surfaces, in-depth understanding of the thermal conditions under which machining-induced SPD layers are generated is still lacking.

Nevertheless, even if not focusing on TSZ, the relationship between thermal fields and microstructural deformation in machining has been considered for the case of PSZ and SSZ. Focusing on PSZ, thermal analysis of SPD in machining of titanium at small-strain rates has shown an analogy between temperature field measured by infrared imaging and strain rate distribution measured by particle image velocimetry [18]. SSZ thermal field analysis has allowed to investigate the role of dynamic recrystallization on the cutting mechanics of AISI 1045 steel, highlighting the microstructural characteristics of cutting regimes presenting formation of built-up edges (BUEs) [19]. Also when cutting advanced nickel-base superalloys, an association between thermal management, machinability and surface integrity has been made, reporting the effect of the gamma prime phase on the alloy strengthening or softening response in cutting [20]. However, the nature of thermal fields experienced by workpiece subsurfaces shearing in TSZ is not very well understood, despite its key relationship with the microstructural deformation and resulting microstructural surface integrity.

Addressing the present gaps within the thermal mechanisms of microstructural surface deformation in machining assumes an even more important role when it comes to the cutting of high temperature superalloys with low machinability and high functional requirements. In fact, powder metallurgy polycrystalline Ni-base superalloys for high-temperature load-bearing applications, such as safety-critical high-pressure discs for the hot stages of aero-engine gas turbines, are among the most advanced materials ever developed [21]. In spite of their crucial role in stepping up the performance of next generation aero-engines, introduction into service of new wrought Ni-base superalloys is an extremely challenging task [22,23], involving in-depth investigation of their physical-chemical behaviour and processability [24,25]. Furthermore, as a result of the unique combination of high-temperature strength and strict quality requirements, machining of

Ni-base superalloys introduces high levels of complexity in all aspects of metal cutting [26].

In spite of the fast-growing knowledge being developed on the microstructural surface integrity induced by mechanical material removal, full comprehension of machined surface metallurgy cannot be achieved without an in-depth understanding of its thermal history.

In this context, the present research aims to bridge the existing gaps

by investigating the thermal history of the material undergoing plastic deformation in the tertiary shear zone (TSZ) and its relationship with the workpiece microstructural surface integrity, considering a development nickel-base superalloy for next-generation aeroengine applications as a case study. This will allow the thermal stages of surface modification to be described, revealing the temperature field evolution within the machining-induced surface deformation process, and the resulting

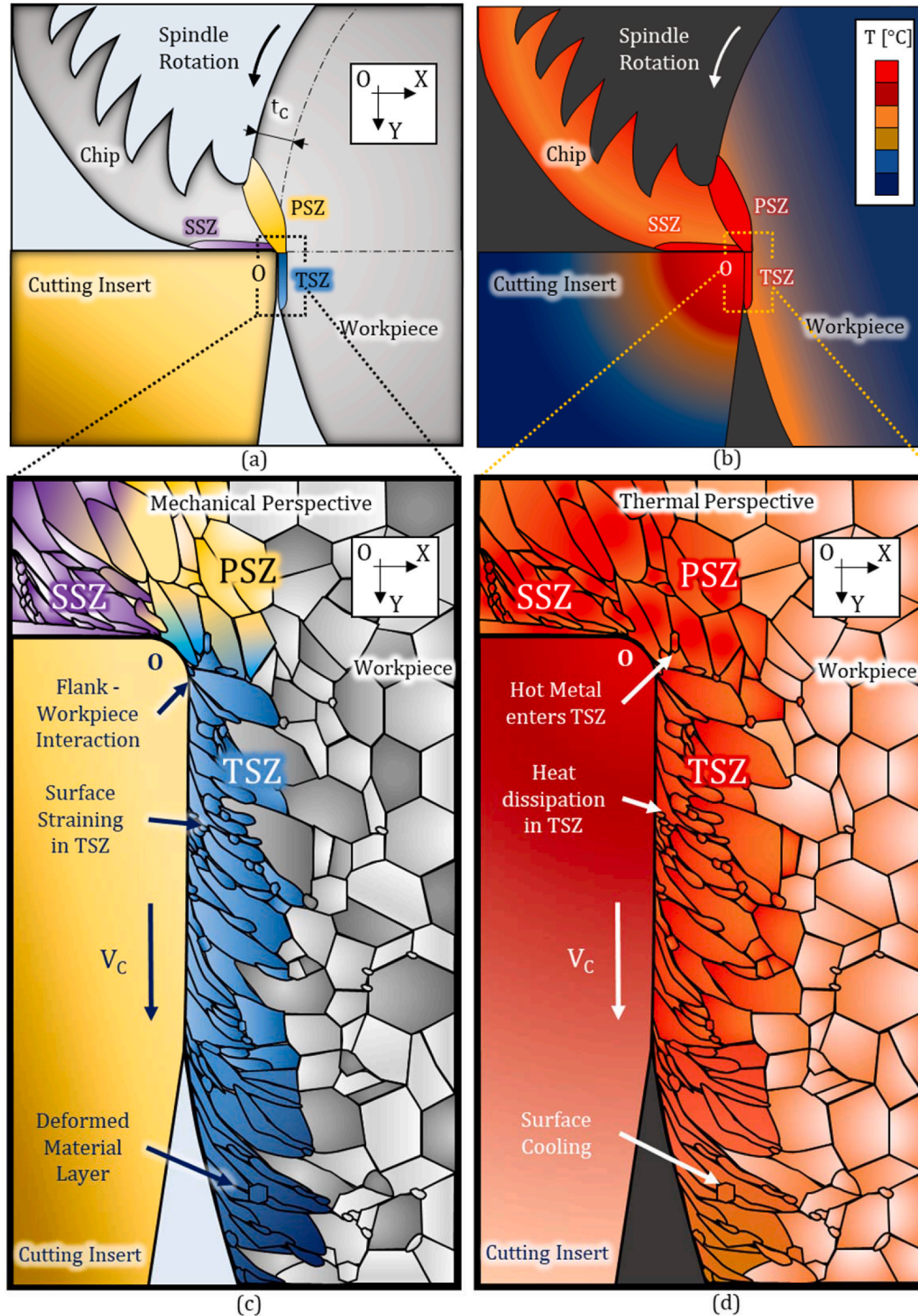


Fig. 1. Schematic representation of the thermo-mechanical conditions in mechanical machining. (a) Mechanical and (b) thermal effects at the tool-workpiece interface, with focus on (c) microstructural workpiece deformation and (d) thermal field development in tertiary shear zone (TSZ) along the flank-workpiece contact length.

subsurface thermal cycles. Moreover, mapping the rates of heat generation in the tertiary shear zone (TSZ) will allow the stages of subsurface plastic deformation to be discussed in relationship to the resulting workpiece microstructural surface integrity.

2. A thermo-mechanical perspective on the machining-induced microstructural surface deformation

To perform mechanical machining processes, plasticity needs to be induced in the workpiece material to be removed and transformed into chips by the action of a cutting insert. However, because of the interaction forces developing at the tool-workpiece interface, deformations can also be induced in the machined part volume, where localised microstructural distortion can be found.

A schematic representation of the thermal and mechanical phenomena evolving at the tool-workpiece interface is provided in Fig. 1. Primary, secondary and tertiary zones developing at the tool-workpiece interface are represented from a mechanical (Fig. 1a,c) and thermal (Fig. 1b,d) perspective with reference to an orthogonal cutting operation.

In PSZ, plastic deformation developing at high rates transforms bulk material layers into a swirling chip, as represented in Fig. 1a,c, generating heat and inducing high-temperatures ahead of the cutter. Furthermore, as each forming chip leaves the cutting zone heavily rubbing against the tool rake, severe shear deformation is induced in SSZ. Concurrently, TSZ deformation occurs in workpiece volumes situated beyond the cutting edge, where friction between the machined surface and the tool flank develops due to the tool-workpiece interaction.

As a result, metallurgical modifications in the machined subsurface can instantaneously occur under high-temperature conditions. As schematically represented in Fig. 1c,d, a material drag (MD) layer presenting a swept grain structure can be induced at shallow depths beneath a machined surface. Moreover, under the most aggressive scenarios, material recrystallization can occur with formation of thin nanocrystalline layers, also known as white layers (WLs), which can extend up to few microns below the newly cut surface.

However, description of the machining-induced mechanical fields or thermal fields is alone unable to provide full description of the generation mechanism of such microstructurally-deformed layers. The material modification occurring in machined subsurfaces has been linked to the extreme strain rates at the tool-workpiece interface, which are in the range of 10^4 - 10^5 s⁻¹ [16,17]. Cutting forces can generally provide only macroscopic indications on the severity of the mechanical fields in machining, which have a global character as they take into account of all the phenomena developing at the tool-workpiece interface, i.e. chip-rake friction, primary shear zone deformation, flank-workpiece forces, and so on. On the other hand, despite the magnitude of machining temperatures can provide information on the severity of a cutting process, it should be noticed that they are inevitably influenced by the local heat transfer boundary conditions (e.g. cutting insert properties, presence of coolant, workpiece conductivity, etc.), and therefore cannot always be used as a metric to compare different cutting scenarios, especially in relationship to the workpiece subsurface deformation.

Therefore, the severity of the mechanical or thermal conditions imposed by the cutting process is in general insufficient to address the resulting workpiece surface integrity, being unable to fully detail the evolving conditions locally developing at the interface between the tool flank and the workpiece surface plastically deforming. In fact, a one-to-one correspondence does not in general exist between such measurements of the thermal or mechanical fields (e.g. cutting forces, cutting temperatures, or strain rates) and the plastic deformation process taking place in the workpiece microstructure. Instead, an energetic description incorporating both the severity of the thermal fields locally developing in the deforming subsurface volumes but also the rates at which such

evolution develops can relate the effect (rates of heat generation and thermal field evolution in TSZ) to its cause (subsurface plastic deformation).

What is hence the relationship between the thermal conditions developing in TSZ and the surface integrity of the machined workpiece? During the interaction of the workpiece surface with the tool flank, plastic deformation in TSZ converts mechanical energy into heat. The metallurgical signature of this process is in fact represented by the workpiece microstructural condition, and thus its surface integrity. It follows that a link must exist between the plastic deformation experienced by the machined workpiece subsurface and the thermal fields developing in the machined part volume, and specifically in TSZ.

As schematically represented in Fig. 1c and d, the transformation of bulk material volumes into machining-affected workpiece layers occurs within their almost instantaneous transition through the tool-workpiece interface (e.g. at 60 m/min, a 0.1 mm distance is crossed in a 10^{-4} s time).

Metal volumes entering TSZ could already present a high temperature after having interacted with the thermal field propagating ahead of the cutter. As the new surface moves past the cutting edge, high-temperature deformation is induced as a consequence of its friction with the tool flank (Fig. 1c). This generates heat through plastic deformation (Fig. 1d), inducing thermal gradients in the workpiece subsurface (Fig. 2). Finally, beyond the region where the tool flank interacts with the workpiece, subsurface deformation no longer occurs (Fig. 1c and d) and the thermo-mechanically affected surface layer cools down while moving away from the cutting zone (Fig. 2a and b).

Specifically, a heating phase is to be expected as the workpiece material approaches the cutting edge location, while cooling must occur as it moves away from this zone. Therefore, continuity of the thermal fields implies that at least one peak of temperature must exist along the workpiece-flank contact length, i.e. between the heating and cooling phases. Moreover, the most severe conditions should occur at shallow surface depths, i.e. in regions passing near the tool flank, with decreasing magnitude moving away from the machined surface (planes $X_1 \dots X_N$ in Fig. 2b and c).

Thus, quick loading-unloading conditions are induced in the workpiece subsurface passing near the tool-workpiece interface. From a mechanical perspective, material shears at high rates (Fig. 1c and d), while from a thermal standpoint the workpiece subsurface undergoes an instantaneous heating-cooling cycle (Fig. 2b and c). Thermal and mechanical fields in TSZ are in truth deeply coupled, as cutting-induced heat generation determines the shape of thermal gradients evolving in the workpiece subsurface, which can in turn influence the high-temperature response of the material volumes plastically deforming.

Therefore, description of space and time evolution of the plastic deformation process in TSZ can be achieved through energy balance analysis. In fact, cutting-induced heat generation results in the formation of high temperature gradients, which induces heat conduction in the workpiece subsurface. Hence, application of thermal balance equations in control volumes located in the tertiary shear zone (TSZ) can allow the distribution of heat generation to be mapped, which enables identification of the stages characterising the subsurface microstructural deformation process.

Thus, open questions that emerge from this analysis include:

- What is the time and space evolution of temperature fields and gradients (Fig. 2a,c) to which workpiece subsurfaces are subject while crossing the tool workpiece interface?
- How is the shape of such thermal cycles (Fig. 2b and c) induced in the workpiece material influenced by thermo-physical boundary conditions in cutting, and what relationship exists between heating and cooling rates experienced by the workpiece subsurface and its microstructural integrity?

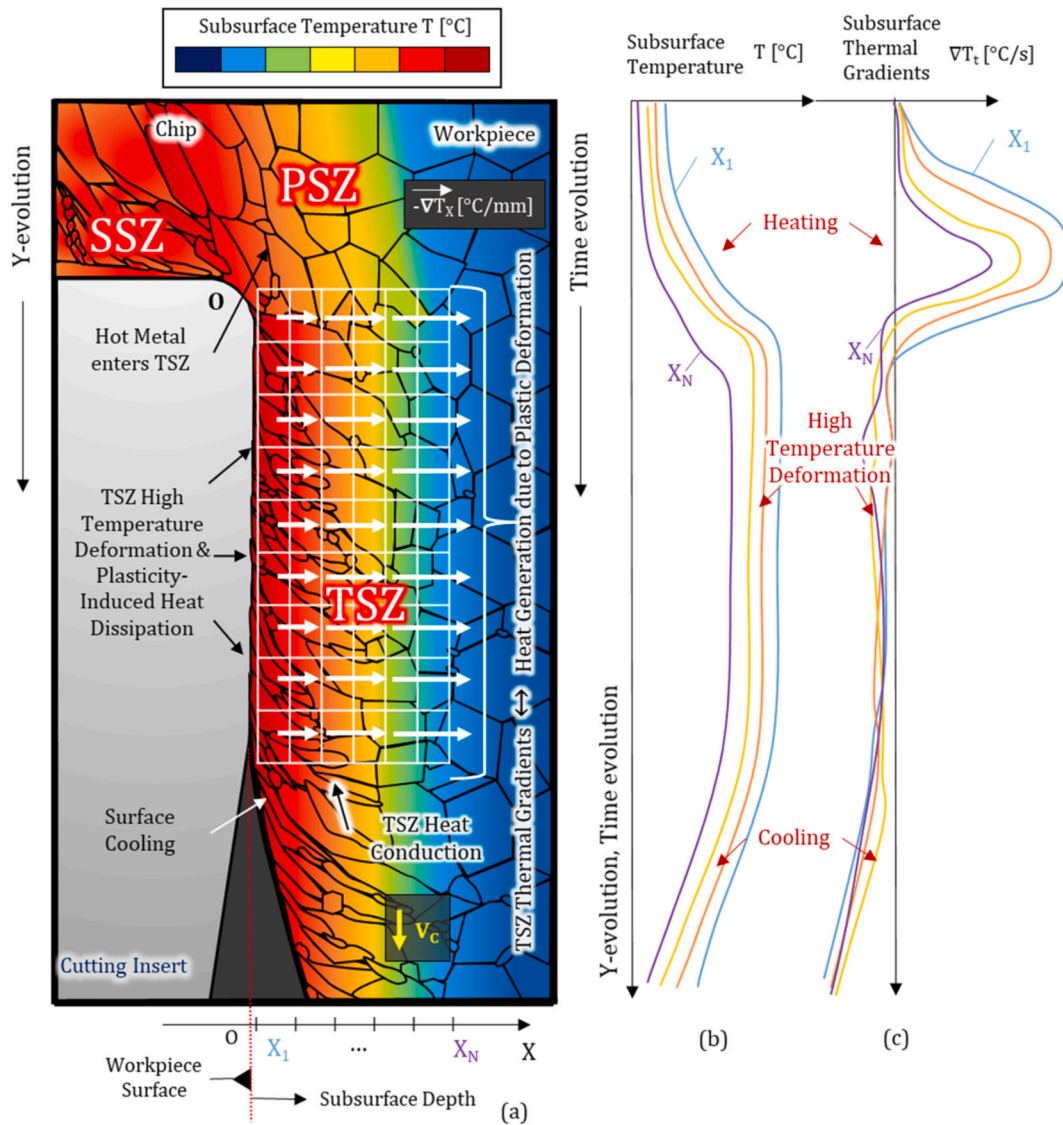


Fig. 2. Schematic representation of the thermal field and temperature gradients evolution in the metal shear zones due to the frictional interaction and plastic deformation developing at the tool-workpiece interface. (a) Subsurface thermal field and spatial thermal gradients induced to the machined surface by the plastic deformation process; (b) temperature and (c) thermal gradients time evolution at different subsurface depths as the workpiece layers cross the tool-workpiece interface, showing heating and cooling phases separated by a high-temperature deformation region. The scheme has been designed to allow a conceptual discussion of a possible thermal field in TSZ, in consistency with the later experimental results.

- Can the analysis of heat generation in TSZ provide information on the formation mechanisms of machining-induced surface layers (e.g. nanocrystalline or MD layers)?

To address these points, the thermal history of microstructural surface deformation is studied under different combinations of mechanical and thermal effects influenced by the selected cutting parameters. This in fact produce different microstructural conditions, which are studied and related to the thermal conditions under which they were produced during the cutting process.

3. Experimental methodology

3.1. Thermal field measurement and machining configuration

The thermal mechanisms of surface deformation in TSZ have been investigated in the context of dry orthogonal cutting experiments, to allow infrared temperature measurement in the cutting zones. More in detail, mechanical machining tests have been carried out under dry

plunge turning conditions employing a grooved workpiece presenting a series of discs with 2 mm thickness separated by 3 mm radial grooves (Fig. 3a and b). In this way, the side edges of the parting tool did not engage with the workpiece while material removal was radially performed (Fig. 3b). Fig. 3c provides a view of the turning set-up with workpiece and cutting insert mounted on the lathe, and a high-speed thermal camera positioned at a controlled distance (2 m) to acquire thermal field measurements of the cutting process in high detail and at high frame rates (650 Hz on a 320×256 pixel window). Under these settings, a 20- μm length corresponds to a pixel unit recorded by the thermal camera, which at the speeds typical of cutting operations is crossed in a very narrow time interval (e.g. in the range of 10^{-5} s for a cutting speeds of 30 m/min). This allows a small-scale analysis of the time and space evolution of thermal fields in the workpiece subsurface, enabling a detailed investigation of the cutting-induced thermal cycles (previously introduced in section 2) under which microstructural deformation is produced. The nominal temperature error for the thermal camera is $\sim 1\%$, to which additional measurement uncertainty adds because of the thermal emissivity assessment, whose evaluation has

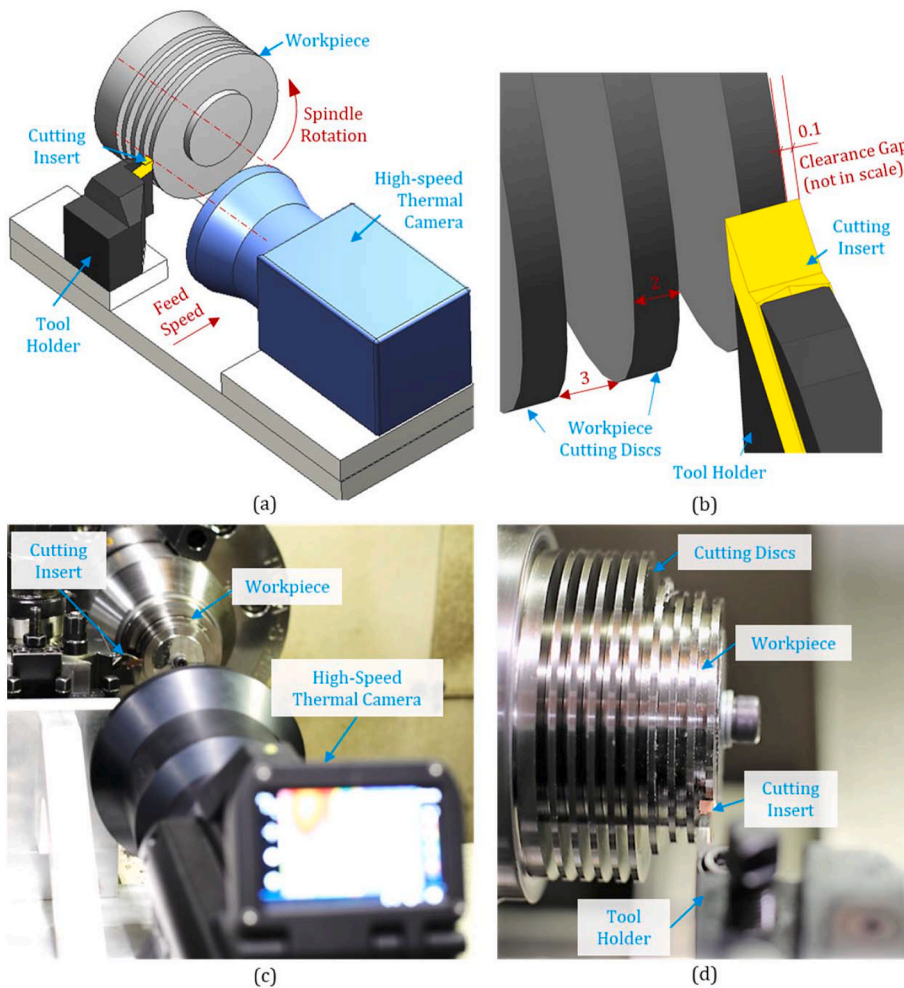


Fig. 3. Experimental set-up for high-speed thermal imaging of the orthogonal cutting process. (a) Schematic of the turning condition with tool-workpiece layout, thermal camera orientation and machine tool kinematics. (b) Workpiece view with detail on cutting discs geometry and tool-workpiece configuration, presenting a 0.1 mm axial clearance. (c) Lathe configuration for high-speed thermal imaging with thermal camera, workpiece material and cutting insert. (d) Workpiece material on which several discs have been generated for orthogonal cutting experiments.

been performed with a precision of ± 0.1 after calibration. Under such conditions, measurement error is typically in the range of 5% [27]. When infrared thermography is employed in metal cutting, temperatures are measured on the outer face of the contact width. Moreover, to limit occurrence of metal side flow, an axial clearance gap of 0.1 mm was allowed between the side faces of the tool and of the workpiece, as shown in Fig. 3b, with an experimental approach similar to the one outlined by Arrazola et al. [28]. This allowed the side flow effect to be limited, making sure that the selected thermal frames were not affected by its presence. In addition, a correction to the thermal maps has been applied in post-processing to estimate thermal conditions reached at the middle zones of the tool-workpiece cutting system, based on previous studies on the three-dimensional temperature field in orthogonal cutting and its measurability by means of infrared thermography [28].

As discussed in Ref. [1], the generation mechanisms of surface integrity in mechanical machining are due to a combination of thermal and mechanical effects developing at the tool-workpiece interface. In particular, mechanical effects are associated to the factors defining the mechanical interference between the cutting tool and the workpiece (e.g. depth of cut, cutting edge radius, flank wear, rake angle, material removal rate, etc.). Differently, thermal effects are associated to the thermal conditions under which material removal, and hence the workpiece plastic deformation, take place (e.g. temperature field, thermal gradients, heating and cooling rates, etc.). Within mechanical machining, these two effects are usually coupled, i.e. the mechanical interaction between the tool and the workpiece has an influence on the thermal field at the tool-workpiece interface, and vice-versa (e.g. due to material temperature softening or hardening behaviour).

In this context, to generate different levels of workpiece microstructural deformation, cutting parameters are selected to modulate the severity of the thermo-mechanical conditions under which the machined surfaces are produced. Specifically, two sets of cutting experiments are considered, which will be referred to as 'conventional' and 'aggressive'. 'Conventional' cutting experiments aim to investigate the deformation process in TSZ when limited amounts of microstructural anomalies and moderate temperature fields are induced. Differently, 'aggressive' cutting experiments aim to study the material deformation in TSZ when much higher levels of microstructural modifications are produced under very high temperatures. In particular, within the study of the machining-induced surface deformation of Ni-base superalloys, aggressive conditions can be associated with extensive subsurface microstructural deformation (e.g. $>20\text{--}25\ \mu\text{m}$), presence of highly refined grain layers (e.g. formation of nanocrystalline layers), extended subsurface depth affected by residual stress, and very high cutting temperatures (e.g. in the range of $10^3\ ^\circ\text{C}$ or above).

Therefore, 'conventional' cutting experiments (Table 1, tests #1 and #2) are performed with inserts presenting a sharp edge radius ($r = 7\ \mu\text{m}$), fresh ($VB_0 = 0\ \text{mm}$), which have been employed at moderate surface speeds (30–70 m/min) and uncut chip thickness (0.1 mm). 'Aggressive' cutting experiments (Table 1, tests #3 and #4) are performed with initially worn tools ($VB_0 = 0.2\ \text{mm}$) having a rounded cutting edge ($r = 30\ \mu\text{m}$), and under higher surface speeds (60–130 m/min) and higher uncut chip thickness (0.15 mm). Hence, because of the higher material removal rates, greater tool radius and higher flank wear, 'aggressive' cutting scenarios are expected to induce a much higher frictional interaction and plastic deformation at the tool-workpiece

Table 1

Set of experiments for thermal field and surface integrity analysis under aggressive and conventional cutting conditions. All insets have neutral rake angle. Conventional conditions employ sharp and fresh cutting edges. Rounded and initially worn inserts have been used in aggressive scenarios.

Test #	Insert grade	Surface Speed (V_c) [m/min]	Feed (f) [mm/rev]	Initial insert condition	Expected Mechanical Effect	Expected Thermal Effect	Cutting condition
1	CC	30	0.1	Fresh ($VB_0 = 0$ mm) Sharp ($r = 7$ μ m)	Low intensity	Medium intensity	Conventional
2	pCBN	70	0.1	Fresh ($VB_0 = 0$ mm) Sharp ($r = 7$ μ m)	Medium intensity	Low intensity	Conventional
3	CC	60	0.15	Worn ($VB_0 = 0.2$ mm) Rounded ($r = 30$ μ m)	High intensity	High intensity	Aggressive
4	pCBN	130	0.15	Worn ($VB_0 = 0.2$ mm) Rounded ($r = 30$ μ m)	Very high intensity	Very high intensity	Aggressive

interface, as it will be later confirmed by the significantly severer cutting temperatures, microstructural deformation and residual stress they induced.

Nevertheless, the thermo-mechanical fields' development at the tool-workpiece interface under a given set of experimental conditions is also expected to be highly dependent on the cutting insert's thermo-mechanical characteristics (e.g. high-temperature hardness, thermal-conductivity, etc.).

Therefore, two key insert materials have been considered to study the behaviour of subsurface thermal fields and its resulting deformation mechanisms, i.e. polycrystalline cubic boron nitride (pCBN) and PVD coated cemented carbide (CC) inserts (CBN170 and TS2050 grades from Seco Tools, respectively). In fact, as pCBN grades present greater hardness with respect to CC ones (even at high temperatures) [29], they are designed to withstand higher cutting speeds, and are hence expected to produce less severe thermal fields even when inducing higher deformation rates to the workpiece subsurface (as in Table 1, tests #1 and #2). In this way, the surface speeds (V_c) adopted under conventional and aggressive experiments have been selected according to the inserts' thermo-physical capability, as shown in Table 1. It should be noted that mechanical and thermal effects are not "separated" in the present experiments, in fact they are coupled effects as mechanical machining is a thermo-mechanical process. However, the differences in cutting conditions (such as tool thermo-physical properties, geometry, uncut chip thickness, etc.), have allowed to design experiments where their relative weight differs. For instance, the different tribological behaviour of CC grades under low cutting speed can induce severer thermal field development at the tool-workpiece interface compared to pCBN, with consequent influence on surface integrity, as it will be discussed in detail in the later experimental section. This allows the workpiece subsurface deformation and the resulting thermal cycles and rates of heat generation in TSZ to be studied under different combinations of thermal and mechanical fields' severity.

3.2. Workpiece material

The development alloy employed in this work as a case study to investigate the thermal history of surface deformation is a next generation polycrystalline nickel-base superalloy for potential application in high-pressure (HP) disc rotors for gas-turbine aero-engines. Details on this material can be found in the patent US10422024B2 [30], including its composition range as reported in Table 2. This nickel-base superalloy is produced by powder metallurgy followed by isothermal forging under controlled temperature, strains and strain rates, to achieve an average grain size of ASTM 8 to 7 (22–32 μ m) [30]. A representative micrograph

displaying the microstructure of the alloy investigated in this research is shown in Fig. 4. Weight fraction of gamma prime phase is a key characteristic of advanced Ni-base superalloys as it confers high temperature strength and determines fatigue crack resistance. The present alloy has gamma prime weight fraction in the range of 51–53%, which is considerably higher than other advanced nickel-base superalloys such as RR1000, whose nominal value is in the range of 45% [23]. Thus, the high content of gamma prime phase with high solvus temperature (<1167 °C [30]) is one of the key aspects that introduce significant challenges when performing mechanical cutting operations of this material.

Therefore, selection of this advanced superalloy provides a unique case study for studying the previously outlined research problem, for the following reasons. First, its advanced high-temperature capability is expected to generate very intense thermo-mechanical fields at the tool-workpiece interface, allowing to study and understand the thermal history of surface deformation when the cutting process is pushed towards its current limits. Moreover, analysis of the thermal history of plastic deformation in this material will contribute to disclose the nature of the physical conditions under which material drag layers and nano-crystalline (white) layers are generated in advanced Nickel-base

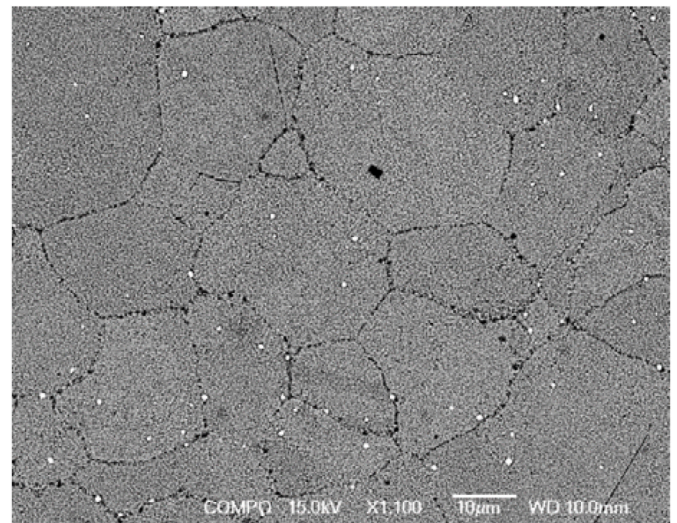


Fig. 4. Scanning electron image showing a representative microstructure of the Ni-base superalloy in 'as received' condition. Sample was chemically etched with Kalling's Reagent No. 2.

Table 2

Composition range for the Ni-base superalloy object of the present research.

wt.%	Ni	Co	Cr	Fe	Mn	Mo	W	Al	Ti	Ta	Nb	Si	C	B	Zr	Hf
min	Bal.	14.6	11.5	0.8	0.2	2.00	3.30	2.90	2.60	3.50	1.20	0.10	0.02	0.010	0.05	0.000
max	Bal.	15.9	13.0	1.2	0.60	2.40	3.70	3.30	3.10	5.10	1.80	0.60	0.06	0.030	0.11	0.045

superalloys, which still represents an open problem at the confluence of metal cutting and material science.

Therefore, to link the thermal conditions evolving in the workpiece volume (in terms of thermal field at the tool-workpiece interface and subsurface thermal cycles) with its resulting microstructural surface integrity, metallurgical analysis of the machining-induced SPD layers has been carried out for each of the scenarios under investigation. To perform microscopy analysis, cross-sections of the machined specimens have been obtained through gradual grinding and polishing steps. Chemical etching was employed to reveal the alloy's microstructure using Kalling's Reagent No.2 consisting of 2% CuCl_2 in an acidified alcoholic base. Subsurface microstructural features have been observed through field emission gun scanning electron microscopy (FEG-SEM) with a JEOL 7000F machine. Electron-Backscatter Diffraction (EBSD) has been employed to investigate the crystallographic lattice condition induced to the machined subsurfaces. EBSD indexing has been performed by means of a Nordlys Max 3 detector (Oxford Instruments), with step sizes smaller than 100 nm (down to 30 nm for the most refined analysis). The resulting inverse pole figure (IPF) and band contrast (BC) maps are presented in 'as-detected' form without application of filtering strategies. In addition, to further detail the surface integrity produced, the residual stress (RS) state in the hoop direction has been characterised within a depth of 350 μm beneath the machined surface for all the cutting scenarios under consideration. RS profiles have been measured through X-Ray Diffraction (XRD) by application of the $\sin^2\psi$ technique, employing a Proto iXRD diffractometer (Mn $K\alpha$ radiation) with an aperture of 1 mm diameter, and 15 kV voltage.

Thus, type and extent of microstructural deformation induced by the cutting process will be linked to the information provided by temperature field maps captured through high-speed thermal imaging. In this way, contextual analysis of the workpiece subsurface condition will be related to the corresponding thermal development at the tool-workpiece interface and to the resulting subsurface thermal cycles, allowing the heat generation in TSZ to be associated to the corresponding mechanism of subsurface plastic deformation during its interaction with the tool flank.

4. Results and discussion

To study the thermal history of microstructural surface deformation, analysis of different combinations of thermal and mechanical effects on the resulting surface integrity will be studied, showing that a more comprehensive description is necessary to address the deformation state induced in the workpiece subsurface. Therefore, a thermo-mechanical description of the process under which subsurface layers deform in cutting will be provided by investigation of the subsurface thermal

cycles and heat generation in TSZ. This will allow the thermal history induced by cutting to be linked to the formation mechanisms of microstructurally deformed layers (MD and WLs) in the workpiece subsurface as a result of the tool-workpiece mechanical interaction induced in the tertiary shear zone (TSZ).

4.1. Influence of the thermo-mechanical cutting configuration on thermal field development at the tool-workpiece interface

4.1.1. Characteristics of the thermal field at the tool-workpiece interface

Analysis of the physical conditions developing at the tool-workpiece interface represents a key element to understand the mechanisms influencing the surface integrity of machined parts. A representative temperature map at the tool-workpiece interface can be observed in Fig. 5a, where an intermediate thermal field severity was generated by means of CC insert employed at moderate surface speed (Test #1, $V_c = 30$, $f = 0.1$). As thermal maps display temperatures above 300 $^\circ\text{C}$, the workpiece volume far (more than $\sim 250 \mu\text{m}$) from the cutting interface (e.g. towards the top-right and bottom-right corners in Fig. 5a) appears to be thermally unaffected (dark blue colour), while high temperature regions can be observed at the tool-workpiece contact region where a chip is forming.

It is at the interface between chip, tool and workpiece that the attention will be focused, as shown in Fig. 5b where the three shear zones (PSZ, SSZ and TSZ) can be thermally identified. A fan of oblique isothermal lines can be observed at the interface between the incoming uncut workpiece material and the cutting edge. In this region, the high-temperature PSZ boundary volume separating workpiece and chip in Fig. 5b highlights the geometrical correspondence between strain localisation areas and shape of the temperature field. Similarly, temperature field can be linked with plastic deformation at the tool-chip interface, where chip deformation develops in SSZ due to the chip-rake friction, and most importantly in correspondence of the TSZ, where the machined surface mechanically interacts with the tool flank, as it will be in-depth discussed in the following sections. Thus, Fig. 6 reports thermal maps corresponding to each of the experiments presented in Table 1 where different combinations of thermal and mechanical effects are induced under conventional (Fig. 6a and b, Tests #1 and #2 in Table 1; $V_c = 30\text{--}70$ m/min, $f = 0.1\text{mm/rev}$, $r = 7 \mu\text{m}$, $VB_0 = 0$ mm), and aggressive scenarios (Fig. 6c and d, Tests #3 and #4 in Table 1; $V_c = 60\text{--}130$ m/min, $f = 0.15\text{mm/rev}$, $r = 30 \mu\text{m}$, $VB_0 = 0.2$ mm). For a straightforward comparison of the magnitude of the thermal fields induced by each cutting condition, thermal maps in Fig. 6 are plotted with the same temperature scale.

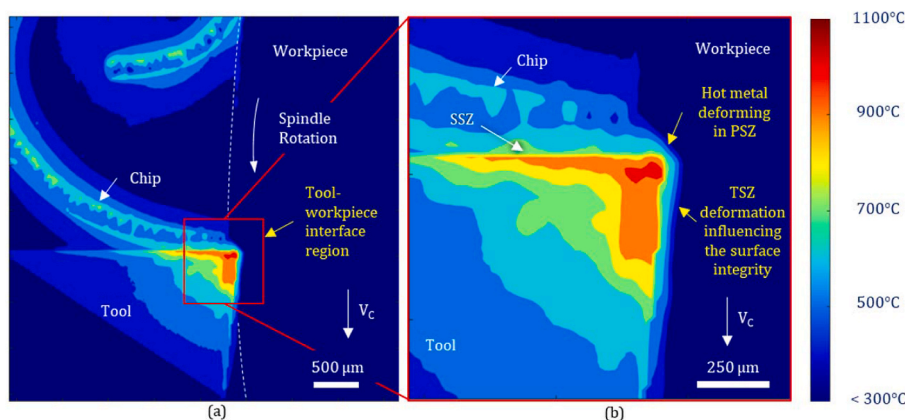


Fig. 5. Example of the tool-workpiece interface temperature map at intermediate thermal field severity (Cutting test #1, $V_c = 30$, $f = 0.1$). (a) Representative characteristics of the cutting-induced thermal field at the tool-workpiece interface. (b) Magnified view at the tool tip area to enable identification of metal shear zones (i.e. PSZ, SSZ and TSZ).

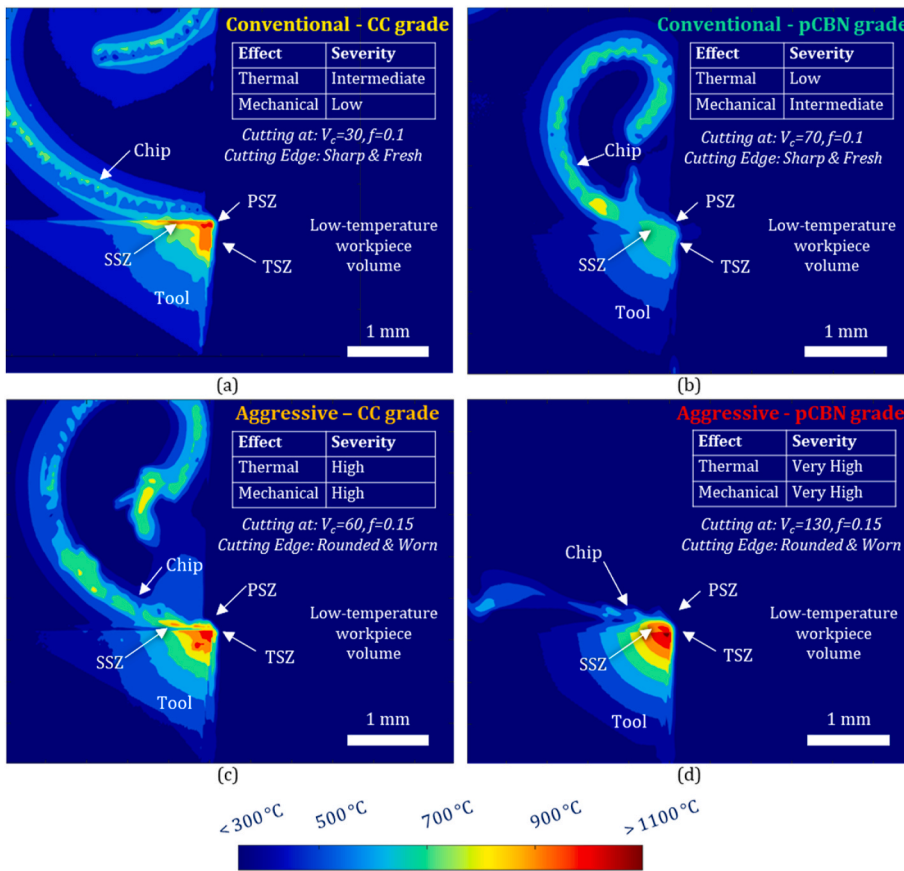


Fig. 6. Thermal maps showing different temperature fields induced when cutting the advanced Ni-superalloy under different combinations of thermal and mechanical effects at the tool-workpiece interface. (a) Intermediate thermal field severity in presence of low-intensity mechanical effects (Test #1: CC insert - $V_c = 30$ m/min, $f = 0.1$ mm/rev, $r = 7$ μ m, $VB_0 = 0$ mm); (b) Lower-intensity thermal fields in presence of mechanical effects of intermediate severity (Test #2: pCBN insert - $V_c = 70$ m/min, $f = 0.1$ mm/rev, $r = 7$ μ m, $VB_0 = 0$ mm); (c) High thermal fields in presence of mechanical effects of high severity (Test #3: CC insert - $V_c = 60$ m/min, $f = 0.15$ mm/rev, $r = 30$ μ m, $VB_0 = 0.2$ mm); (d) Very high thermal fields in presence of mechanical effects of extreme severity (Test #4: pCBN insert - $V_c = 130$ m/min, $f = 0.15$ mm/rev, $r = 30$ μ m, $VB_0 = 0.2$ mm).

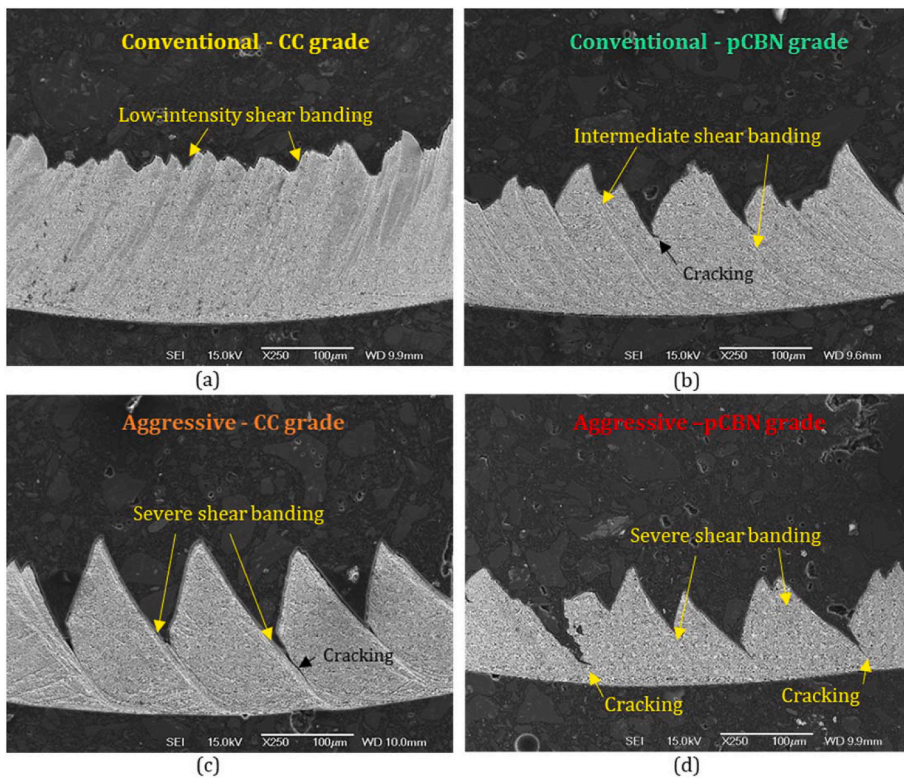


Fig. 7. Chip morphology induced when cutting the advanced Ni-superalloy under different combinations of thermal and mechanical effects at the tool-workpiece interface. (a) Mild shear banding induced by a combination of intermediate thermal effects and low-intensity mechanical effects (Test #1: CC insert - $V_c = 30$ m/min, $f = 0.1$ mm/rev, $r = 7$ μ m, $VB_0 = 0$ mm); (b) Intermediate shear banding induced by a combination of low-intensity thermal effects and intermediate mechanical effects (Test #2: pCBN insert - $V_c = 70$ m/min, $f = 0.1$ mm/rev, $r = 7$ μ m, $VB_0 = 0$ mm); (c) Severe shear banding induced by a combination of high thermal and mechanical effects (Test #3: CC insert - $V_c = 60$ m/min, $f = 0.15$ mm/rev, $r = 30$ μ m, $VB_0 = 0.2$ mm); (d) Severe shear banding with almost separated chip segments induced by a combination of very high thermal and mechanical effects; (Test #4: pCBN insert - $V_c = 130$ m/min, $f = 0.15$ mm/rev, $r = 30$ μ m, $VB_0 = 0.2$ mm).

4.1.2. Tool-workpiece interaction under moderate thermo-mechanical effects

Even though it operated under the least severe mechanical conditions ($V_C = 30$ m/min, $f = 0.1$ mm/rev, $r = 7$ μ m, $VB_0 = 0$ mm), among the conventional scenarios in Fig. 6a and b cutting performed with the CC grade induced highest tool-tip temperatures is (Fig. 6a). In this context, temperatures recorded for the CC insert (in the range of 900 °C in Fig. 6a) are higher than the ones induced by the pCBN ones (in the range of 700 °C in Fig. 6b). This despite the fact that pCBN inserts were employed under more severe mechanical conditions and in particular at a surface speed more than two times higher ($V_C = 70$ m/min, $f = 0.1$ mm/rev, $r = 7$ μ m, $VB_0 = 0$ mm). This could be attributed to the different tribological conditions developing at the tool workpiece interface, with carbide tools undergoing significant adhesion both in the flank region and at the tool-chip interface when turning Ni-base superalloys [16,31]. On the other hand, when cutting with pCBN inserts, the higher cutting speed resulted in higher deformation rates at the tool-workpiece interface, as it can be qualitatively appreciated from the more pronounced shear banding induced in the chip formation process when the pCBN tool was used (Fig. 7b) with respect to the CC one (Fig. 7a). Therefore, the thermal and mechanical conditions under which new machined surfaces are generated in these two cases present remarkably different characteristics: in the first case, higher temperature fields were produced at the tool workpiece interface by CC under conventional cutting conditions, even though the deformation process was induced at slower rates (Figs. 6a and 7a). On the contrary, cutting at higher speeds with pCBN inserts induced higher rates of deformation at the tool-workpiece interface, although under milder thermal conditions (Figs. 6b and 7b).

What is hence the influence of such different combinations of thermal and mechanical effects on the resulting workpiece integrity? Moreover, which description of the cutting-induced physical effects is more appropriate to address the workpiece subsurface deformation process? To address this, the following sections will first characterise the nature and extent of microstructural deformation induced to the workpiece, and then examine the time and space evolution of thermal field induced in workpiece surficial layers as they cross the cutting zone. In this way, thermal cycles induced by such combinations of thermal and mechanical effects will be linked to the corresponding microstructural surface integrity.

4.1.3. Tool-workpiece interaction under severe thermo-mechanical effects

Differently from conventional cutting configurations, aggressive cutting scenarios (Fig. 6c and d) are purposely designed to investigate the tool-workpiece interaction process under thermal and mechanical effects of higher severity, achieved by employing a more frictional cutting geometry ($r = 30$ μ m; $VB_0 = 0.2$ mm) and under higher rates of material removal (Tests #3 and #4 in Table 1). Under such conditions, cutting temperatures above 1000 °C have been widely reached in such aggressive cutting scenarios (Fig. 6c and d). However, if under the moderate/intermediate mechanical effects characterising conventional cutting experiments pCBN inserts were able to produce a more tolerable thermal field severity at over twice the surface speeds of CC grades (with pCBN having tool-tip temperatures about 200 °C lower), the same trend is not found under more aggressive cutting conditions. In fact, when performing aggressive cutting, pCBN inserts operated at maximum tool tip temperatures above 1100 °C (Fig. 6d), condition under which they were still able to withstand the stress field necessary to cut workpiece material at high removal rates from the advanced Ni-base superalloy under consideration, thanks to their exceptional high-temperature hardness [32]. Moreover, the severity of mechanical and thermal effects induced by aggressive cutting configurations in the metal deforming at the tool-workpiece interface can be also qualitatively appreciated by the high levels of segmentation induced in the resulting chips, as displayed in Fig. 7c and d. In fact, high temperature and high strain rate conditions induced by aggressive cutting experiments

resulted in short and highly serrated chips, indicating occurrence of severe strain localisation ahead of the cutter, in which proximity material layers about to form the new (machined) surface transit before their mechanical interaction with the tool flank.

As a result, severe shear banding can be observed in Fig. 7c for the case of CC aggressive cutting ($V_C = 60$ m/min, $f = 0.15$ mm/rev, $r = 30$ μ m, $VB_0 = 0.2$ mm), with high-temperature strain localisation in chips induced by aggressive cutting with pCBN tools ($V_C = 130$ m/min, $f = 0.15$ mm/rev, $r = 30$ μ m, $VB_0 = 0.2$), presenting almost separated segments in Fig. 7d. Thus, thermal history of machining-induced SPD layers will be in this way investigated also under severe levels of tool-workpiece thermo-mechanical interaction. Specifically, even though aggressive and conventional experiments presented different mixes of thermal and mechanical effects, a unified description is needed to coherently address the subsurface deformation under the conditions examined.

To this aim, the microstructural surface integrity will be first characterised in terms of type and extent of machining-induced SPD layers for the different experimental cases. Subsequently, the subsurface thermal cycles for aggressive cutting will be investigated, linked to the workpiece microstructural state, and analysed in relationship to the thermal history induced by conventional experiments. Finally, taking an aggressive cutting scenario as a case study, energy balance analysis will allow the stages of plastic deformation in the workpiece subsurface to be outlined.

4.2. Microstructural analysis of the cutting-induced subsurface deformation as a result of different combinations of thermal and mechanical effects

Since the workpiece loading in mechanical machining originates at the tool-workpiece interface, the most-severe microstructural deformation is produced at the lowest depths beneath the newly cut surface [1]. In previous sections, it has been discussed how different severity of thermal and mechanical effects coexisted under conventional cutting scenarios, with higher temperatures reaching ~ 900 °C at the tip of CC inserts at 30 m/min, in contrast with the ~ 700 °C reached by pCBN ones at 30 m/min. Moreover, a system of much more extreme thermo-mechanical conditions was induced by aggressive cutting experiments, with cutting temperatures above 1100 °C at speeds up to 130 m/min induced at the tool-workpiece interface. Therefore, the question now focuses on what the outcome of such systems of thermal and mechanical effects will be on the resulting surface integrity, and most importantly, how their thermal history can be addressed and related to the corresponding subsurface states.

In analogy with the severity of thermal and mechanical effects discussed in 4.1, the microstructural integrity of surfaces generated under conventional and aggressive scenarios also present very distinct properties. When comparing the surface deformation induced under low/intermediate thermo-mechanical conditions (conventional cutting experiments), material drag (MD) layers in a range of 11–15 μ m (Fig. 8) and similar RS-affected depths (Fig. 11) were generated by pCBN and CC insert grades. Such MD values are in fact relatively far from the 24–28 μ m extent and type of microstructural deformation produced by aggressive cutting, which induced both MD and WLs in the workpiece subsurface (Fig. 9) and severer RS states (Fig. 11), as reported by the surface integrity plot in Fig. 10.

In truth, observation of MD layers induced by conventional cutting with CC and pCBN grades (Fig. 8a,c) reveals the existence of very similar material states despite the previously mentioned different combinations of thermal and mechanical effects. Both cases show in fact presence of a crammed series of narrow strain traces originating at the machined surface and propagating with increasing inclination towards higher material depths, as displayed by the detail views in Fig. 8b,d. This microstructural condition is associated with high lattice distortion [11] resulting from cutting-induced plasticity. Moreover, it is noted how an

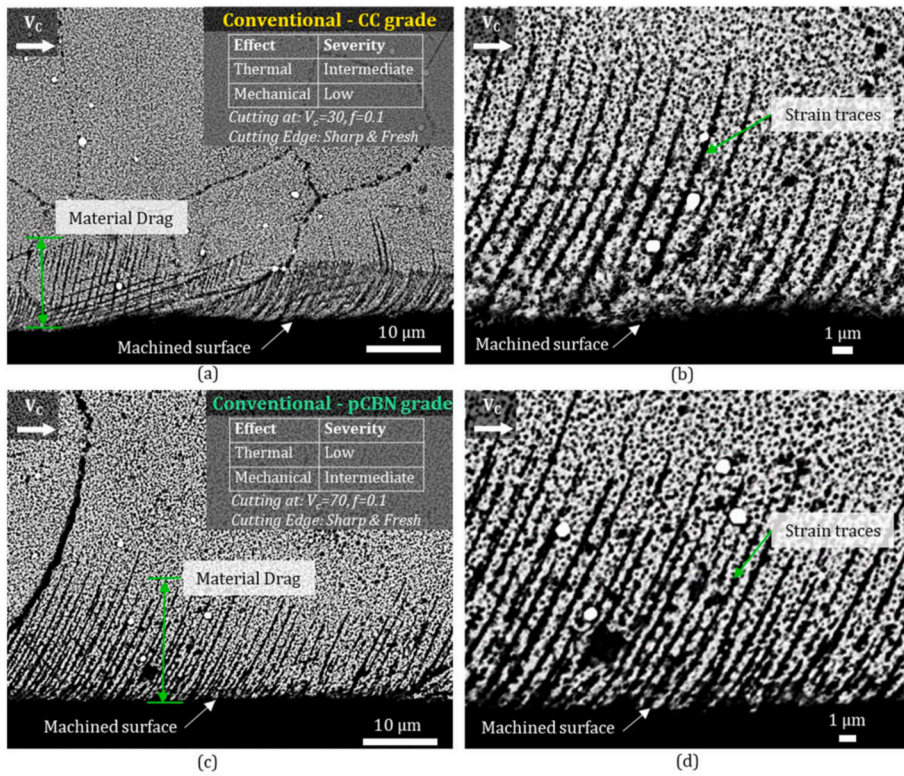


Fig. 8. Microstructural surface integrity resulting from conventional cutting conditions. (a) Material Drag induced by intermediate thermal effects and low-intensity mechanical effects (Test #1: CC insert - $V_c = 30$ m/min, $f = 0.1$ mm/rev, $r = 7 \mu\text{m}$, $VB_0 = 0$ mm); (b) Detail of the strain traces induced by low-intensity thermal effects and intermediate mechanical effects in the workpiece subsurface (Test #1: CC insert - $V_c = 30$ m/min, $f = 0.1$ mm/rev, $r = 7 \mu\text{m}$, $VB_0 = 0$ mm); (c) Material Drag induced by moderate thermal effects and intermediate mechanical effects (Test #2: pCBN insert - $V_c = 70$ m/min, $f = 0.1$ mm/rev, $r = 7 \mu\text{m}$, $VB_0 = 0$ mm); (d) Detail of the strain traces induced by moderate thermal effects and intermediate mechanical effects (Test #2: pCBN insert - $V_c = 70$ m/min, $f = 0.1$ mm/rev, $r = 7 \mu\text{m}$, $VB_0 = 0$ mm).

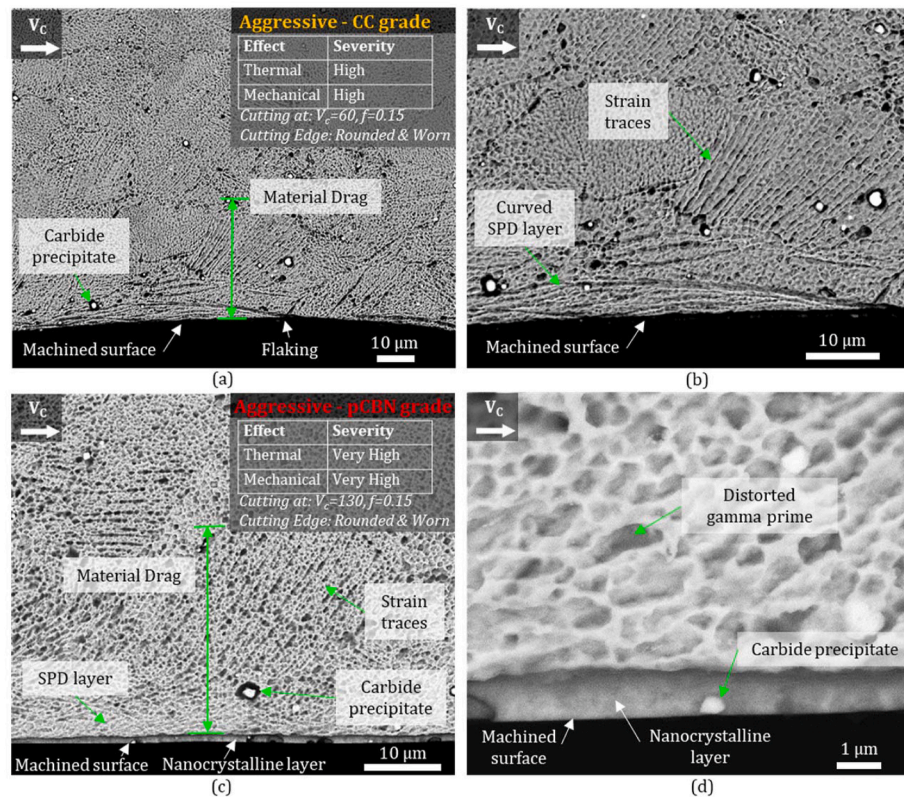


Fig. 9. Microstructural surface integrity resulting from aggressive cutting conditions. (a) Material Drag induced by high thermal and mechanical effects (Test #3: CC insert - $V_c = 60$ m/min, $f = 0.15$ mm/rev, $r = 30 \mu\text{m}$, $VB_0 = 0.2$ mm); (b) Detail of the strain traces induced by high thermal and mechanical effects in the workpiece subsurface (Test #3: CC insert - $V_c = 60$ m/min, $f = 0.15$ mm/rev, $r = 30 \mu\text{m}$, $VB_0 = 0.2$ mm); (c) Material Drag induced by extreme thermal and mechanical effects (Test #4: pCBN insert - $V_c = 130$ m/min, $f = 0.15$ mm/rev, $r = 30 \mu\text{m}$, $VB_0 = 0.2$ mm); (d) Detail of the strain traces induced by extreme thermal and mechanical effects (Test #4: pCBN insert - $V_c = 130$ m/min, $f = 0.15$ mm/rev, $r = 30 \mu\text{m}$, $VB_0 = 0.2$ mm).

11 μm MD layer has been induced under thermal fields of intermediate severity but coexisting with low-intensity mechanical effects induced by cutting at 30 m/min with a CC insert, which is not far from the 15 μm

induced at a surface speed of 70 m/min by the pCBN grade, under more pronounced mechanical effect but a less severe temperature field. In fact, it had been previously commented how the CC tool tip resulted

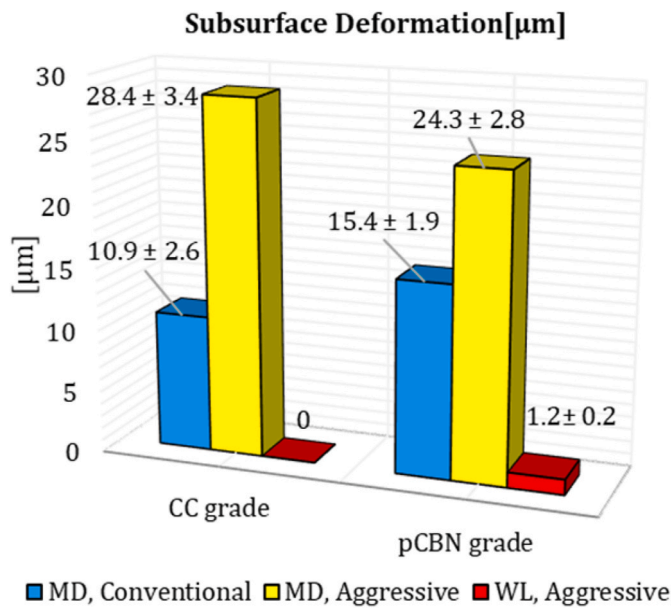


Fig. 10. Type and extent of microstructural deformation for each cutting scenario in terms of Material Drag (MD) layers from conventional and aggressive scenarios and White Layers (WLs) from aggressive scenarios (no WLs were generated under conventional conditions). Relatively close ranges of MD are observed after conventional cutting experiments despite the different combinations of thermal and mechanical field severity induced by such scenarios, with a much deeper metallurgical reconfiguration instead observed under high severity of thermal and mechanical fields induced by aggressive experiments.

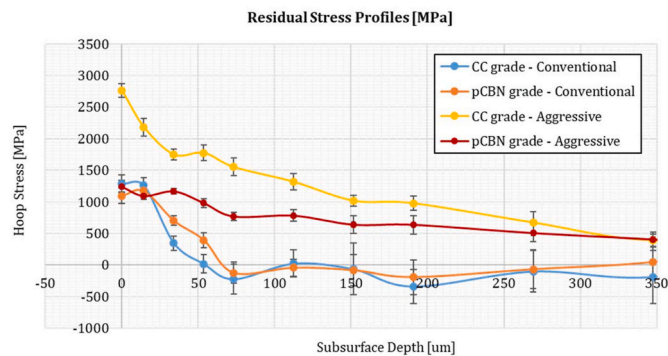


Fig. 11. Residual Stress (RS) profiles for each cutting scenario measured in the hoop direction. Relatively close depths of material affected by tensile RS are observed after conventional cutting experiments despite the different combinations of thermal and mechanical field severity induced by such scenarios. A much more extended depth of tensile RS is found as a result of the high severity of thermal and mechanical fields induced by aggressive experiments.

~200 °C hotter, even though lower rates of deformation were induced with respect to pCBN, as qualitatively indicated by the greater chip serration induced by the latter. As the insert geometries in these two cases were identical, the only factors influencing this behaviour are cutting speeds and insert thermo-physical properties. Additionally, this is supported by examination of the EBSD maps in Fig. 12a and b. In fact, presence of similar crystal lattice distortion and grain sweep is found at shallow depths beneath the machined surfaces produced by Test #1 (CC grade cutting at 30 m/min) and Test #2 (pCBN cutting at 70 m/min), with modest grain refinement and formation of sub-grains (Fig. 12b and c). From a RS perspective (Fig. 11), it can be seen how for both CC and pCBN cases under ‘conventional’ conditions the presence of tensile RS is

limited within similar subsurface depths (~55–65 μm). Thus, despite the apparently different thermo-mechanical conditions at the tool-workpiece interface, relatively comparable outputs were produced in terms of microstructural deformation and residual stress (RS) state. Hence, to provide a more appropriate interpretation of the mechanisms generating such microstructural deformation, further attention should be focused on the analysis of the thermal conditions in TSZ, with a description comprising both the cutting-induced thermal field and the rate at which the process develops.

Differently, a more severe metallurgical condition is found as a result of the thermo-mechanical effects induced by aggressive cutting experiments, with microstructurally deformed regions propagating over subsurface depths beyond ~25 μm (Fig. 9). In these regions, the intense thermal effects induced by aggressive cutting with CC inserts (tool-tip temperatures above 1000 °C) coupled with highly-frictional flank-workpiece interaction ($V_C = 60$ m/min, $f = 0.15$ mm/rev, $r = 30$ μm, $VB_0 = 0.2$ mm) has resulted in material drag (MD) layers extending for up to ~28 μm, together with the formation of curved SPD layers and surface micro-flaking, as shown in Fig. 9a and b. From a RS perspective (Fig. 11), aggressive cutting conditions produced residual tensile loading with values above 600 MPa for over 200 μm beneath the machine surface. In particular, it is noted how high hoop RS were induced by CC inserts under aggressive conditions, with values in excess of 2500 MPa at the surface level. These are indeed remarkably high values, which can relate to the results from Herbert et al. [32], where RS over 2000 MPa were found in RR1000 after aggressive drilling. Possibility of reaching such RS values could be attributed to the mechanical properties of machining-induced SPD layers in Ni-base superalloys, e.g. as reported in Refs. [17,20] where stresses over 2000 MPa were measured under uniaxial micro-mechanical loading. However, it should be observed that the constitutive behaviour of machining-induced SPD layers still represents an open topic of research. In addition, an even more anomalous microstructural condition is found when examining the subsurface cut under extreme combinations of temperature field severity (with temperatures above 1100 °C) and tool-workpiece mechanical engagement ($V_C = 130$ m/min, $f = 0.15$ mm/rev, $r = 30$ μm, $VB_0 = 0.2$ mm), in correspondence of aggressive cutting tests with pCBN grades, as shown by the cross-sectional surface micrograph in Fig. 9c. In fact, a wide MD layer propagating up to depths beyond ~24 μm is found to coexist with a thin recrystallized nano-grain layer, also known as white layer (WL), attached to the machined surface with a thickness above 1 μm, as displayed by the near-surface detail view in Fig. 9d. This highly refined layer presents fully dissolved gamma prime precipitates [17] with occasional embedment of carbide particles that eventually withstood the severe deformation process. Moving at higher depths in the machined surface, the microstructural deformation state gradually decreases its severity, indicating that the cutting process induced remarkably distorted but not fully dissolved gamma prime particles just few microns above the nanocrystalline layer inner boundary, as shown in Fig. 9 d.

More insights on the machining-induced surface state resulting from severe thermo-mechanical effects are provided by analysis of the EBSD maps in Fig. 13 (Test #4: pCBN insert - $T_{MAX} > 1100$ °C at $V_C = 130$ m/min, $f = 0.15$ mm/rev, $r = 30$ μm, $VB_0 = 0.2$ mm). Specifically, Fig. 13a shows IPF and BC maps over a relatively large area, covering a subsurface depth that is greater than the extent of MD previously observed by secondary electron imaging. On one hand, this shows how the most-severe microstructural distortion was produced at shallow subsurface depths, as further highlighted by the lowering in BC quality in Fig. 13b in the corresponding regions. However, detailed observation of Fig. 13a reveals that less-severe changes in intra-grain crystallographic texture are present even at depths beyond the previously assessed MD depth, e.g. at the confluence of the grain boundaries (GBs) towards the top-middle of Fig. 13a (in dark blue, light blue/cyan and light purple colours). Hence, although SEM imaging of etched surfaces allows to identify the depth of material presenting the most severe microstructural distortion, more refined approaches such as EBSD are required to

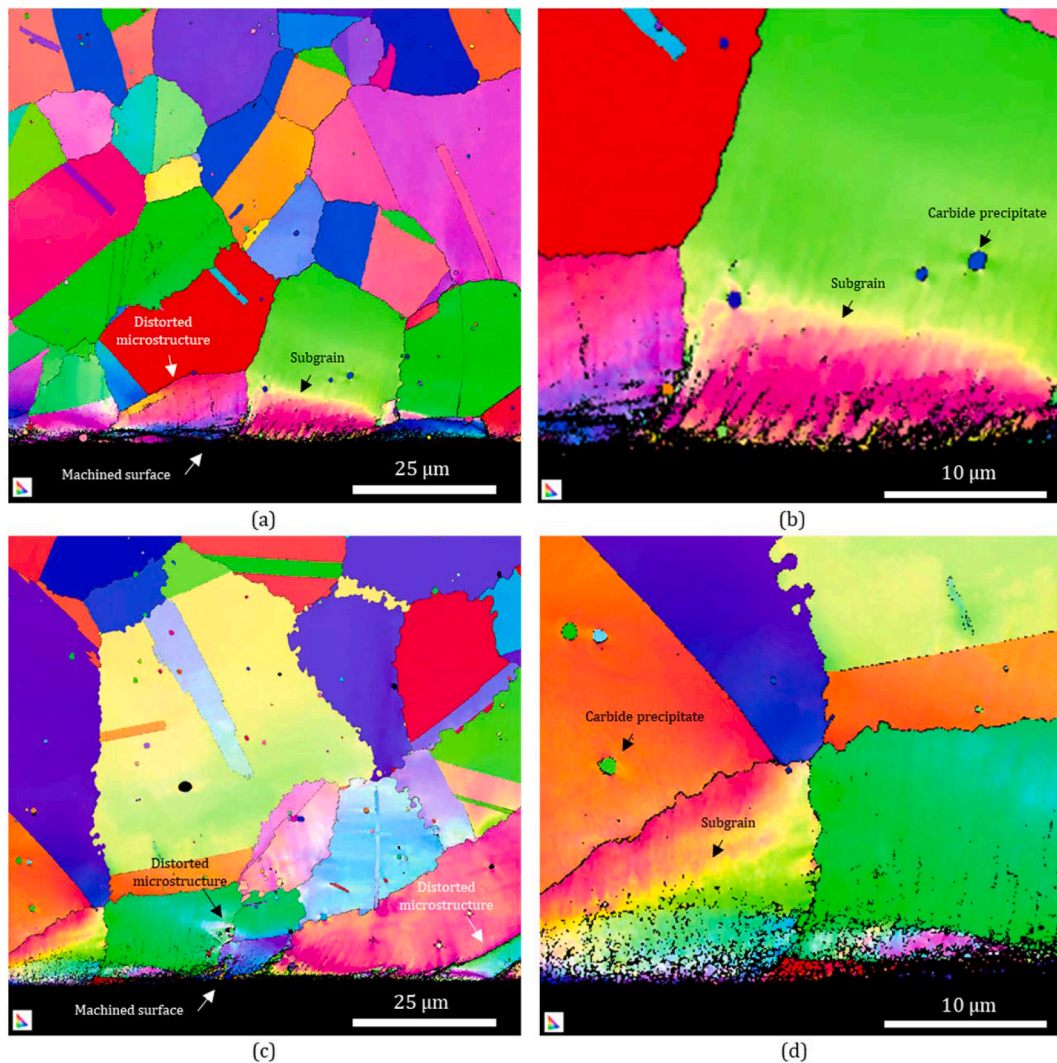


Fig. 12. Subsurface lattice condition observed through EBSD indexing detailing the mildly distorted microstructural state induced by conventional cutting experiments. (a) Microstructural condition induced by intermediate thermal effects and low-intensity mechanical effects (Test #1: CC insert - $V_C = 30$ m/min, $f = 0.1$ mm/rev, $r = 7$ μ m, $VB_0 = 0$ mm); (b) Detail of the near-surface crystallographic condition induced by low-intensity thermal effects and intermediate mechanical effects in the workpiece subsurface (Test #1: CC insert - $V_C = 30$ m/min, $f = 0.1$ mm/rev, $r = 7$ μ m, $VB_0 = 0$ mm); (c) Microstructural condition induced by moderate thermal effects and intermediate mechanical effects (Test #2: pCBN insert - $V_C = 70$ m/min, $f = 0.1$ mm/rev, $r = 7$ μ m, $VB_0 = 0$ mm); (d) Detail of the near-surface crystallographic condition induced by low-intensity thermal effects induced by moderate thermal effects and intermediate mechanical effects (Test #2: pCBN insert - $V_C = 70$ m/min, $f = 0.1$ mm/rev, $r = 7$ μ m, $VB_0 = 0$ mm).

observe the more subtle plastic deformation taking place at higher depths beneath the machined surface. Furthermore, detail views of the microstructural condition in the very proximity of the machined surface are provided in Fig. 13c and d. Significant microstructural distortion is in fact revealed in Fig. 13c, with presence of highly bent microstructure and grain refinement down to the nanoscale at the most-shallow surface depths. Even more detailed information on the texture induced in these regions can be obtained by analysis of Fig. 13d, showing how the strain localisation pattern fragmented bigger grains into progressively smaller ones of sub-micron size.

Thus, when it comes to aggressive scenarios, the influence of the severe thermal and mechanical effects on the subsurface metallurgical condition appears to be of clearer interpretation. As reported by the plot in Fig. 10, despite the high thermo-mechanical effects ($T_{MAX} > 1000$ °C at $V_C = 60$ m/min, $f = 0.15$ mm/rev, $r = 30$ μ m, $VB_0 = 0.2$ mm) induced by aggressive cutting with CC inserts induced similar extent of material drag as pCBNs with MD layers in the range of 24–28 μ m, the extreme temperatures and mechanical aggressiveness induced by pCBN inserts ($T_{MAX} > 1100$ °C at $V_C = 130$ m/min, $f = 0.15$ mm/rev, $r = 30$ μ m, $VB_0 =$

0.2 mm) resulted in a much deeper metallurgical reconfiguration in the workpiece subsurface because of the additional presence of WLs having ~ 1 μ m thickness.

In fact, formation of nanocrystalline layers as the one in Fig. 9 d in advanced Nickel-base superalloys is in fact associated to extreme thermo-mechanical conditions. As discussed in Ref. [17], WL generation in this class of materials takes place by instantaneous dissolution of gamma prime precipitates, which is accompanied by submicron recrystallization induced by the high dislocation densities developing as the subsurface deforms. The aforementioned research work further indicates that the heating and cooling rates experienced by the subsurface are accounted significant influence on the gamma prime precipitation and grain recrystallization process. However, no clear description of the nature of such heating and cooling cycles exists to explain the thermal field dynamics developing within the machined subsurfaces of advanced Ni-base superalloys as they deform at the tool-workpiece interface.

To address these key points, the following sections will investigate the temperature gradients developing in the machined surface volume when crossing the tool-workpiece interface region. Analysis of the time

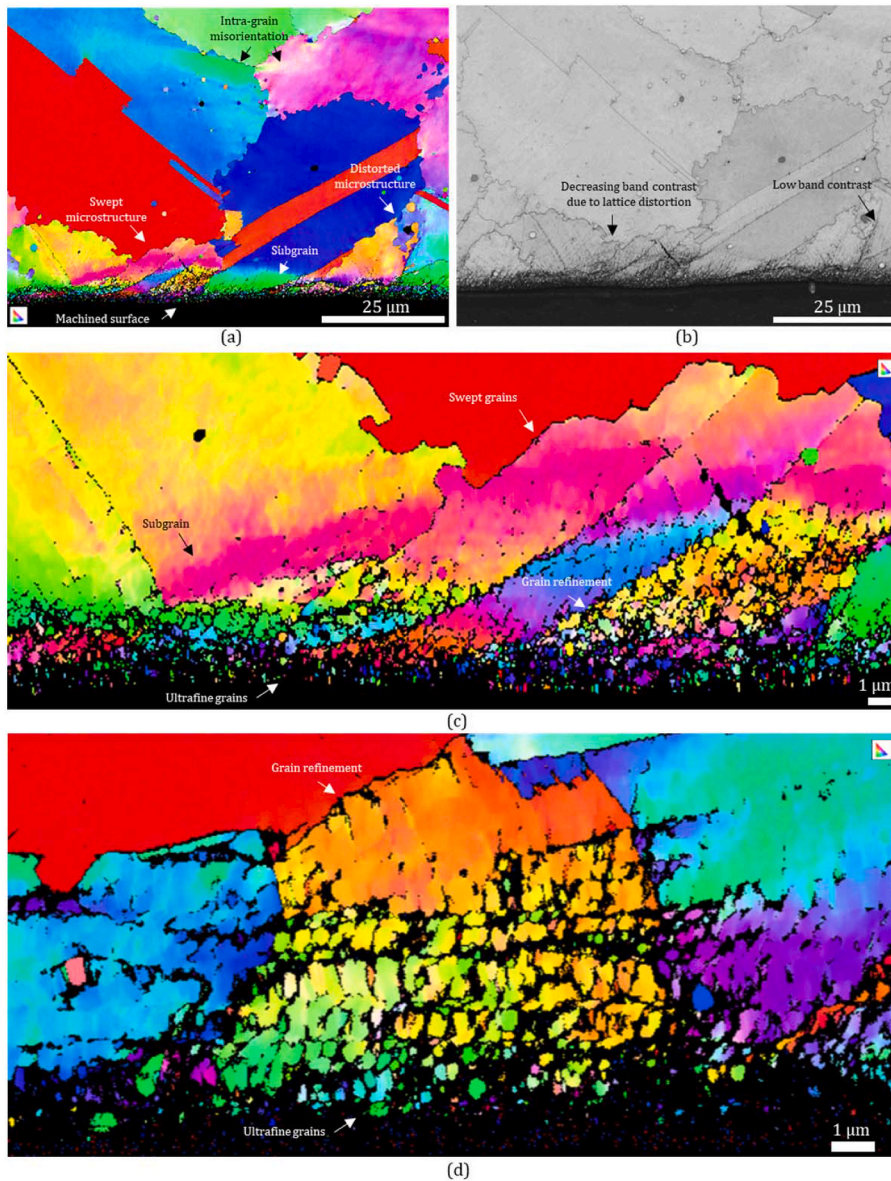


Fig. 13. Subsurface lattice condition observed through EBSD indexing detailing the highly distorted microstructural state induced by aggressive cutting experiments (Test #4: pCBN insert - $V_C = 130$ m/min, $f = 0.15$ mm/rev, $r = 30$ μ m, $VB_0 = 0.2$ mm). (a) IPF map showing highly distorted microstructure with decreasing severity moving away from the machined surface. (b) BC map showing decreasing pattern contrasts moving towards the machined surface due to high lattice distortion in these areas. (c) Near surface IPF map detailing highly bent microstructural condition and grain refinement. (d) High-detail EBSD map (30 nm step size) showing the deformation pattern in the near surface region with sub-micron grain refinement.

and space evolution of the temperature field will thus allow the nature of thermal cycles experienced by the workpiece subsurface to be quantified and related to the corresponding workpiece microstructural integrity. Finally, thermal balance analysis will be carried out to understand the rate of heat generation in TSZ allowing discussion of the thermal stages of subsurface deformation when cutting this unique class of materials.

4.3. Subsurface thermal cycles under thermo-mechanical effects of intermediate severity

Different combinations of mechanical and thermal effects have been observed as a result of conventional cutting experiments with pCBN (lower thermal effects but higher rates of deformations) and CC inserts (lower mechanical effects but higher cutting temperatures), which however produced type and extent of subsurface deformation in comparable ranges (~ 11 – 15 μ m). Therefore, for a more in-depth understanding of the thermo-mechanical process transforming bulk material into microstructurally deformed regions, the thermal history of the workpiece subsurface needs to be considered with a description taking into account of both the severity of the cutting-induced thermal fields, but also of the rates at which the process is performed.

To this aim, a reference system OXY is defined as follows. The origin O is placed at the projection of the cutting edge on the cutting plane; the Y-axis parallel and concordant with the cutting speed vector; and the X-axis is perpendicular to Y and oriented from the tool towards the machined surface, as shown by the referencing adopted in Fig. 14a. To study the thermal cycle experienced by mechanically affected workpiece layers, the cylindrical workpiece geometry is approximated as planar in regions near the flank-workpiece interface. Thus, the workpiece subsurface is regarded as linearly translating along Y, with a uniform velocity equal to the surface speed V_C relative to the cutting insert. In this way, neglecting the effect of local fluctuations induced by strain-dependent kinematics and unsteady temperature components with respect to mean value measurements, thermal field evolution in time (t) can be obtained from its spatial distribution. In fact, in contraposition to continuous chip formation, unsteady thermal conditions with high frequency fluctuations should be expected at the tool-workpiece interface within the formation of serrated chips as the ones shown in Fig. 7. However, within the scope of the present analysis, these high frequency components are neglected and mean values measurements obtained by thermal imaging are considered. Consequently, Fig. 14a shows the trace of four 20 μ m-spaced planes, whose projection identifies the streamlines

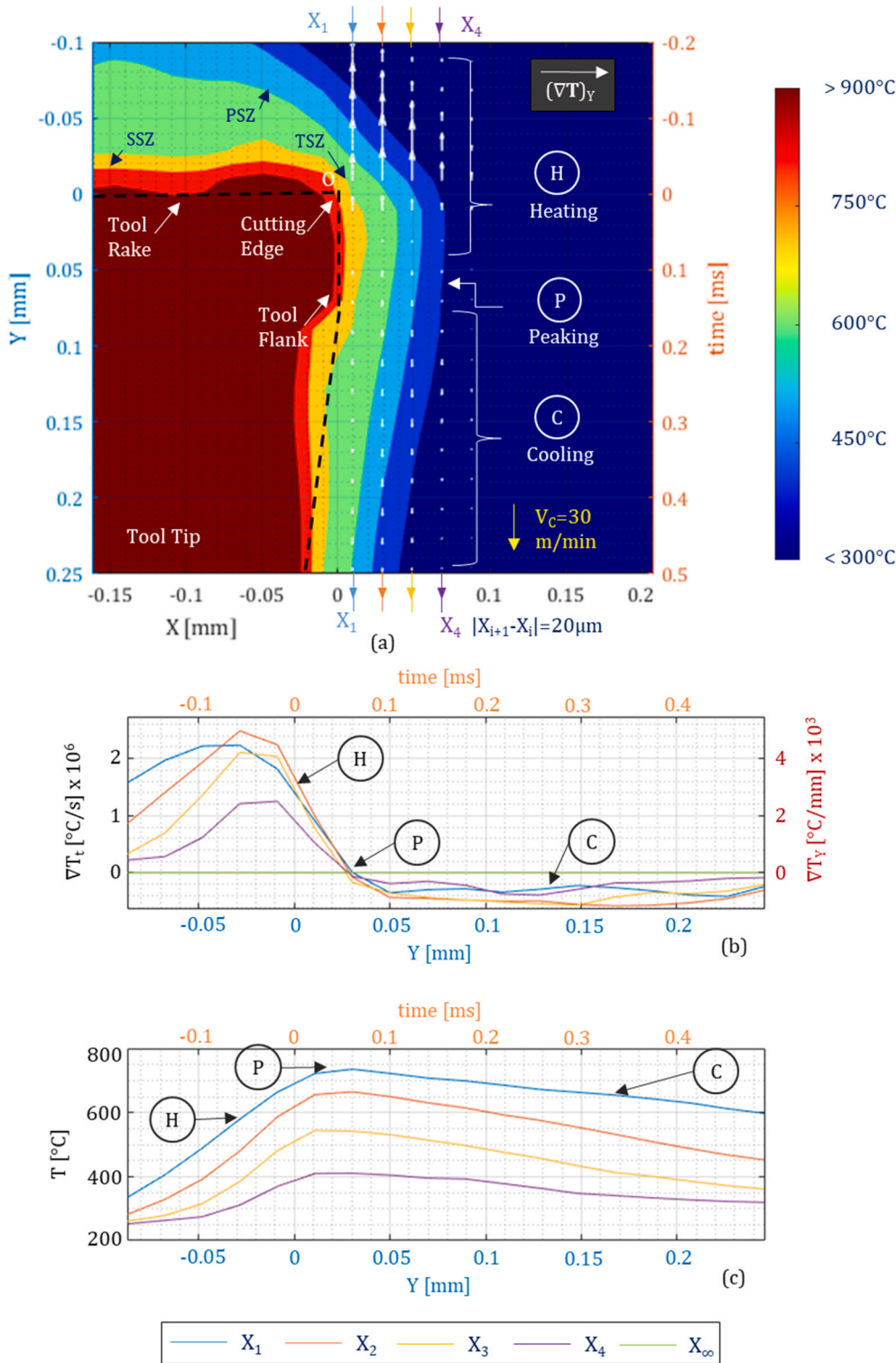


Fig. 14. Subsurface thermal history induced by low-intensity thermal effects and intermediate mechanical effects (Test #1: CC insert - $V_C = 30$ m/min, $f = 0.1$ mm/rev, $r = 7$ μ m, $VB_0 = 0$ mm) for different stages of the thermal cycle: H - heating, P - peaking, C - cooling along streamlines X₁ - X₄; (a) Thermal micrograph at the tool-workpiece interface. (b) Subsurface thermal gradients in time (∇T_t [°C/s] - left vertical axis) and space (∇T_Y [°C/mm] - right vertical axis) at increasing subsurface depths (X [mm], streamlines X₁ - X₄). (c) Subsurface temperature profiles (T [°C]) in time and space at increasing subsurface depths (X [mm], streamlines X₁ - X₄).

X₁ to X₄. These lines indicate the trajectory followed by workpiece regions crossing the tool-workpiece interface at increasing distances from the cutting insert. As these trajectories are described along Y at speed V_C, the distribution of temperature at each streamline X₁, ..., X₄ provides an indication of the thermal cycle experienced at different workpiece subsurface depths while crossing the tool-workpiece interface.

Thus, Fig. 14a presents a thermal field map detailing the area of interaction between the workpiece and the flank under intermediate thermal effects (tool tip temperature ~900 °C) and low-intensity

mechanical effects (V_C = 30 m/min, f = 0.1 mm/rev, r = 7 μ m, VB₀ = 0 mm) induced by conventional cutting with a CC insert. The Y component of the temperature gradient (∇T_Y) is reported in this figure at different depths beneath the workpiece surface corresponding to the streamlines previously introduced, whose distribution has been plotted in Fig. 14b. Applying the known law of motion of the workpiece subsurface, time evolution of thermal gradients (∇T_t) is plotted in Fig. 14b. Similarly, temperature distribution (T [°C]) can be found for each streamline X₁, ..., X₄ as a function of time and along Y in Fig. 14c.

Following the evolution of these quantities along the X_i paths, the thermal cycle experienced by the workpiece subsurface at each tool pass can be regarded as the following three-step process.

- (i) **Heating (H):** as bulk material approaches the cutting zone, thermal field propagating ahead of the tool-workpiece interface induces extreme thermal gradients resulting in ultra-rapid subsurface heating. As shown in Fig. 14b, maximum values of thermal gradients along Y reach above $4000\text{ }^\circ\text{C}/\text{mm}$, corresponding to heating rates over $2 \times 10^6\text{ }^\circ\text{C}/\text{s}$ at depths beyond $60\text{ }\mu\text{m}$ beneath the machined surface. The transition of the workpiece subsurface through these regions hence induces an increase in temperature of $\sim 400\text{ }^\circ\text{C}$ after moving of ca. $150\text{ }\mu\text{m}$ in a time of $\sim 0.2\text{ ms}$ (Fig. 14c).
- (ii) **Peaking (P):** Even though temperature gradients present different heating rates along each of the streamlines X_i , they all reach zero almost simultaneously after surpassing the cutting edge (Fig. 14b). This corresponds to a narrow time interval where the temperature at each streamline reaches its peak (Fig. 14c), occurring at a Y-distance of $\sim 50\text{ }\mu\text{m}$ beyond the cutting edge.
- (iii) **Cooling (C):** Moving further away from the cutting zone, thermal gradients become negative (Fig. 14b) with decreasing temperatures at all depths in the workpiece subsurface (Fig. 14c). Cooling rates experienced by machining-induced material layers appear to be much smaller in absolute value than the heating rates induced ahead of the cutting edge, with values approaching $-0.5 \times 10^6\text{ }^\circ\text{C}/\text{s}$ in time, corresponding to Y gradients of $\sim -1000\text{ }^\circ\text{C}/\text{mm}$.

The above Heating, Peaking, Cooling (H–P–C) thermal cycle is not symmetrical, as the heating rates are about four times higher than the cooling rates. The highest temperature location in the peaking zone (along the Y axis) is associated with the location where highest heat generation occurs along the tool-flank contact, from where thermal power is conducted to the surrounding metal volumes. From a material perspective, the Y coordinate where temperature peaks indicates the location where the most severe plastic deformation occurs in TSZ along the flank contact. For the scenario examined in Fig. 14, this corresponds to a distance of approximately $50\text{ }\mu\text{m}$ from the cutting edge. As a wear length of $\sim 90\text{ }\mu\text{m}$ was later measured on the tool flank, this suggests that a significant amount of tool-workpiece interaction, and hence workpiece microstructural deformation, further occurred beyond the peaking zone. This effect slows down the cooling phase in the workpiece subsurface thermal cycle and contributes to the asymmetry of the thermal plots in Fig. 14b and c with respect to the peaking location. However, even though the temperature peak location can be associated with the greatest source of heat generation due to plastic deformation, distributions of thermal gradients cannot be directly linked to plasticity over the whole XY domain, as they are also influenced by local heat transfer conditions, especially due to heat conduction within the workpiece volume. This is proven by the fact that high heating/cooling rates were found up to $60\text{--}80\text{ }\mu\text{m}$ depths in the workpiece surface, which did not undergo too significant plastic deformation as no traces of strain were found by microstructural material analysis over a $10\text{ }\mu\text{m}$ depth. Nevertheless, the magnitude of thermal gradients experienced by the workpiece subsurface is found to relate well with the resulting surface condition, being an indirect consequence of the amount of heat generated by plastic deformation at the tool-workpiece interface.

In this regard, the previously analysed subsurface thermal cycle resulting from a moderate mechanical effect but higher thermal fields (CC cutting with tool tip temperature $\sim 900\text{ }^\circ\text{C}$ at $V_C = 30\text{ m/min}$, $f = 0.1\text{ mm/rev}$, $r = 7\text{ }\mu\text{m}$, $VB_0 = 0\text{ mm}$) is now compared with the case which instead involved a greater mechanical influence but a less severe thermal effect (pCBN cutting with tool tip temperature $\sim 700\text{ }^\circ\text{C}$ at $V_C = 70\text{ m/min}$, $f = 0.1\text{ mm/rev}$, $r = 7\text{ }\mu\text{m}$, $VB_0 = 0\text{ mm}$). In fact, despite such differences in thermo-mechanical boundary conditions at the tool

workpiece interface, it has been remarked how these scenarios produced subsurface deformation in relatively close ranges ($11\text{--}15\text{ }\mu\text{m}$), as well as similar depths of material presenting a tensile RS state ($55\text{--}65\text{ }\mu\text{m}$). Thus, to shed light on the physical conditions under which surface deformation is generated, analysis of the cutting-induced subsurface thermal cycle is carried out also for latter scenario.

In fact, when considering the H–P–C thermal cycle (Fig. 15b and c) induced to the workpiece subsurface as a result of lower thermal boundary conditions but imposed at higher rates (due to the higher surface velocity in pCBNs cutting), the resulting thermal evolution presents similarities with the one produced by more severe thermal conditions, but induced at lower velocities (CCs conventional cutting - Fig. 14b and c).

In fact, Fig. 15a shows that the milder thermal effect associated to pCBN cutting conditions induced Y-temperature gradients up to $\sim 2500\text{ }^\circ\text{C}/\text{mm}$, lower than the $\sim 4000\text{ }^\circ\text{C}/\text{mm}$ to CC ones. However, when taking into account the time element, i.e. the rate at which this thermal evolution takes place, it is in truth found that higher heating rates are induced by pCBN cutting experiments in the workpiece subsurface, even in correspondence of a remarkably colder tool-tip temperature ($\sim 200\text{ }^\circ\text{C}$ lower than to CCs). As a result, peaks above $3 \times 10^6\text{ }^\circ\text{C}/\text{s}$ are found to be induced by the thermo-mechanical conditions generated by pCBN cutting (Fig. 15a), which are higher but in comparable range with the $2 \times 10^6\text{ }^\circ\text{C}/\text{s}$ heating rates induced by CCs at 30 m/min (Fig. 14b). This corresponds to a temperature peak in a range of $\sim 750\text{ }^\circ\text{C}$ also for pCBNs, which is reached at a Y-distance from the cutting edge of $\sim 85\text{ }\mu\text{m}$ (Fig. 15b). However as the cutting speed is in this case significantly higher, temperature cycles under this condition develop under shorter times (Fig. 15b), representing from a different perspective the higher rates of deformation induced to the material subsurface.

4.4. Subsurface thermal cycles under severe thermo-mechanical effects

An extreme class of thermo-mechanical phenomena has been observed when the cutting process is pushed towards its limits under aggressive machining conditions. As previously detailed, these scenarios are characterised by acute chip serration, high cutting temperatures ($>1100\text{ }^\circ\text{C}$ at the insert tip), formation of extensive material drag layers (up to $\sim 28\text{ }\mu\text{m}$) and a nanocrystalline layers ($>1\text{ }\mu\text{m}$) in the most severe cases, with high depths of material presenting a tensile RS state ($>200\text{ }\mu\text{m}$ at over 600 MPa).

To study the mechanisms governing this class of phenomena, thermal cycles induced by aggressive machining conditions are now taken into account. Fig. 16a presents a thermal map focusing on the interaction between the cutting insert and the workpiece subsurface within the experiment performed under very high thermal and mechanical effects (pCBN cutting with tool tip temperature $\sim 1100\text{ }^\circ\text{C}$ at $V_C = 130\text{ m/min}$, $f = 0.15\text{ mm/rev}$, $r = 30\text{ }\mu\text{m}$, $VB_0 = 0.2\text{ mm}$). In addition, time and space evolution of thermal gradients and temperature field along the streamlines X_1, \dots, X_4 are reported in Fig. 16c,b, respectively. Compared to the phenomena revealed by analysis of non-aggressive cutting scenarios, the three-stage thermal cycle experienced by the workpiece subsurface differs not only in magnitude of the heating/cooling rates, but a quasi-isothermal deformation region is observed where conventional cutting conditions induced a narrow peaking region.

Hence, thermal cycles induced by aggressive cutting are described by the following phases:

- (i) **Heating (H):** bulk material approaching the cutting zone undergoes to increasing heating rates that reach values over $10^7\text{ }^\circ\text{C}/\text{s}$ (Fig. 16b), hence about one order of magnitude higher than the ones induced by conventional cutting scenarios. Maximum values of thermal gradients along Y are above $5000\text{ }^\circ\text{C}/\text{mm}$ (Fig. 16b), with the workpiece subsurface experiencing an increase in

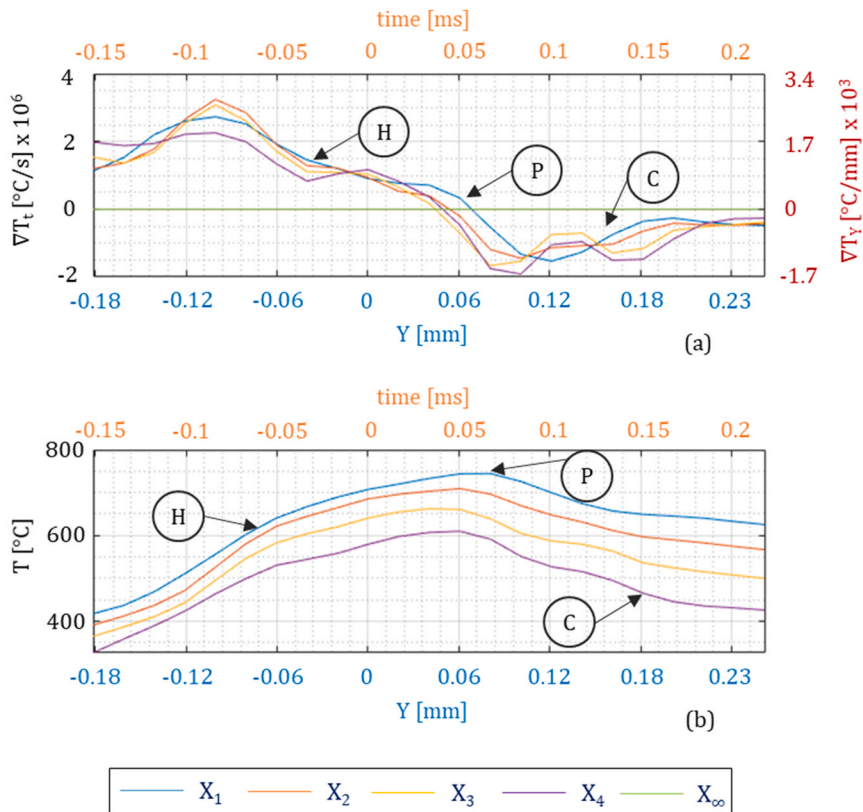


Fig. 15. Subsurface thermal history induced by moderate thermal effects and intermediate mechanical effects (Test #2: pCBN insert - $V_c = 70$ m/min, $f = 0.1$ mm/rev, $r = 7$ μ m, $VB_0 = 0$ mm) for different stages of the thermal cycle: H – heating, P - peaking, C - cooling; (a) Thermal micrograph at the tool-workpiece interface. (b) Subsurface thermal gradients in time (∇T_t [°C/s] - left vertical axis) and space (∇T_y [°C/mm] - right vertical axis) at increasing subsurface depths (X [mm], streamlines $X_1 - X_4$). (c) Subsurface temperature profiles (T [°C]) in time and space at increasing subsurface depths (X [mm], streamlines $X_1 - X_4$).

temperature greater than 800 °C, which occurs over a distance of ~ 250 μ m covered in a time just below 0.15 ms (Fig. 16c).

- (ii) **Quasi-Isothermal Deformation (Q):** Temperature peaks are reached beyond the cutting edge location, where plastic deformation develops in TSZ, with a maximum temperature approaching 1000 °C at the streamline X_1 closest to the tool flank. However, differently from conventional cutting scenarios, while moving along Y (i.e. parallel to the tool flank) thermal gradients remain close to zero for a length of ~ 200 μ m at each streamline X_i , as shown by Fig. 16b. This indicates that at these scales the material deformation taking place in the workpiece subsurface develops under quasi-isothermal conditions over time at each level X_i along the flank-workpiece contact region, as shown in Fig. 16c.
- (iii) **Cooling (C):** Finally, at distances over 200 μ m beyond the cutting edge, temperature starts decreasing at all subsurface depths (Fig. 16c). Thermal variations in the cooling region occurs at a much slower pace than in the heating step, resulting in cooling rates down to -2×10^6 °C/s, corresponding to thermal gradients in Y in the range of -1000 °C/mm (Fig. 16b).

Thus, under this system of extreme thermo-mechanical conditions, the narrow peaking zone previously observed under conventional cutting conditions is replaced by a broader high-temperature region in correspondence of the workpiece-flank contact, which separates the heating and cooling phases. This hence indicates that at constant subsurface depths, i.e. at constant X -locations in Fig. 13, the microstructural deformation previously observed by surface integrity analysis developed under quasi-isothermal conditions.

Under this scenario, the previously mentioned asymmetry of the H-P-C cycle recorded under conventional conditions degenerated into a finite quasi-isothermal deformation zone developing once the temperature peak has been reached, with a Heating, Quasi-Isothermal Deformation, Cooling (H-Q-C) thermal cycle. It should be noted that for the

case presented in Fig. 16, the Quasi-Isothermal Deformation zone extends over a length of ~ 200 μ m, which is comparable with the initial tool wear of the insert employed for this experiment ($VB_0 = 0.2$ mm - Test #4 in Table 1). Hence, the existence of such Quasi-Isothermal Deformation region is attributed to the longer contact length inducing the peaking zone (previously observed in the H-P-C thermal cycles) to extend over a larger region. Coherently with conventional scenarios, also under aggressive conditions the magnitude of thermal gradients relates with the severity of microstructural subsurface deformation, as the heat enabling existence of subsurface thermal gradients is generated by cutting-induced plastic deformation.

Nevertheless, as previously observed for conventional scenarios, also under aggressive conditions high thermal gradients are found at subsurface depths up to ~ 80 μ m, far from the ~ 30 μ m depth where the most-severe microstructural deformation was observed by material analysis. Thermal-cycle analysis is hence able to provide information on the location where most intense deformation occurs (temperature peak location) and on the “overall” severity of the plastic deformation process, as the thermal gradients relate with the extent of subsurface deformation layers. However, this approach is still unable to fully detail the evolution of plasticity over the flank-workpiece interaction. Therefore, to understand the stages of subsurface plastic deformation, the heat generation developing in TSZ will be analysed in the following section by means of an energy balance approach.

4.5. Heat generation in tertiary shear zone in relationship to the mechanisms of microstructural surface deformation

The subsurface thermal cycles described in the previous sections are a result of heat generation taking place as the workpiece material plastically deforms. To understand the time and space evolution of plasticity in the workpiece subsurface, the amount of heat dissipated by this irreversible process is studied by means of thermal balance analysis in material volumes situated beyond the cutting edge, where the

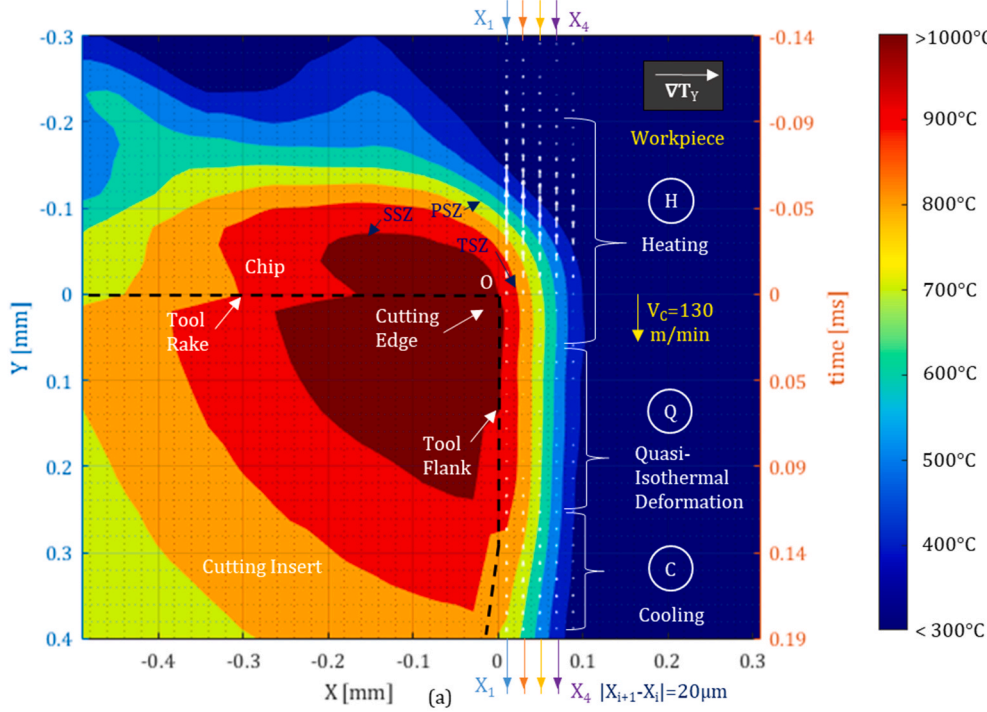
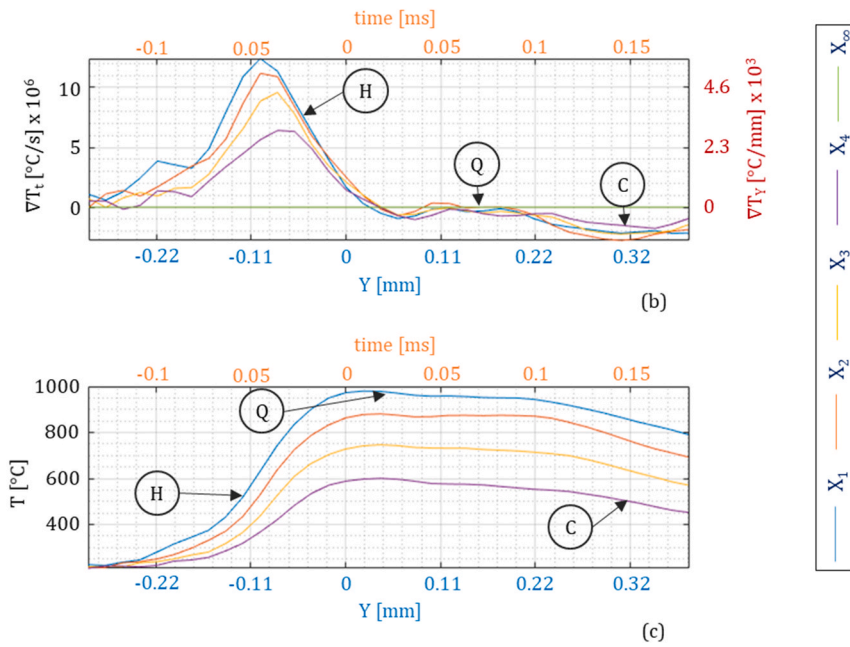


Fig. 16. Subsurface thermal history induced by extreme thermal and mechanical effects (pCBN insert; $V_c = 130$ m/min, $f = 0.15$ mm/rev, $r = 30$ μ m, $VB_0 = 0.2$ mm) for different stages of the thermal cycle: H - heating, Q - Quasi-isothermal deformation, C - cooling along streamlines $X_1 - X_4$; (a) Thermal micrograph at the tool-workpiece interface. (b) Subsurface thermal gradients in time (∇T_t [$^{\circ}\text{C}/\text{s}$] - left vertical axis) and space (∇T_y [$^{\circ}\text{C}/\text{mm}$] - right vertical axis) at increasing subsurface depths (X [mm], streamlines $X_1 - X_4$). (c) Subsurface temperature profiles (T [$^{\circ}\text{C}$] in time and space at increasing subsurface depths (X [mm], streamlines $X_1 - X_4$).



workpiece surface mechanically interacts with the tool flank.

As discussed in the previous section, a quasi-isothermal deformation zone with $\nabla T_y \sim 0$ exists at the flank-workpiece contact under aggressive cutting conditions. As a consequence, isothermal curves in this region can be assimilated to line segments parallel to the Y -axis, i.e. to the machined surface trace on the cutting plane (Fig. 16a). As the thermal gradient field is locally perpendicular to isothermal lines, the vector $\vec{\nabla T}(X, Y)$ is with good approximation parallel to the X -axis versor \vec{e}_x , as expressed by Eq. (1):

$$\vec{\nabla T}(X, Y) \cong \vec{\nabla T}_x(X, Y) \stackrel{\text{def}}{=} \frac{\partial T(X, Y)}{\partial X} \vec{e}_x \quad (1)$$

To apply thermal balance equations in the subsurface area, the TSZ domain is discretized through a mesh of control volumes, as shown in

Fig. 17. In performing this analysis, unsteady (high-frequency) components are neglected with respect to mean value measurements of the thermal field. Hence, the time variations reported in the following are a result of the workpiece subsurface motion in a thermal field regarded as steady. For each control volume V_{ij} located at (X_i, Y_j) , the energy balance equation can be written as:

$$\dot{E}_{gen}(X_i, Y_j) = \dot{E}_{out}(X_i, Y_j) - \dot{E}_{in}(X_i, Y_j) \quad (2)$$

where \dot{E}_{in} represents the rate of energy in entrance, \dot{E}_{out} the energy rate flowing away, and \dot{E}_{gen} the rate of heat being generated in the control volume centred in (X_i, Y_j) . Hence, Eq. (2) states that if the rate of thermal energy leaving the control volume is greater than one in entrance, their difference is equal to the rate of thermal energy being generated.

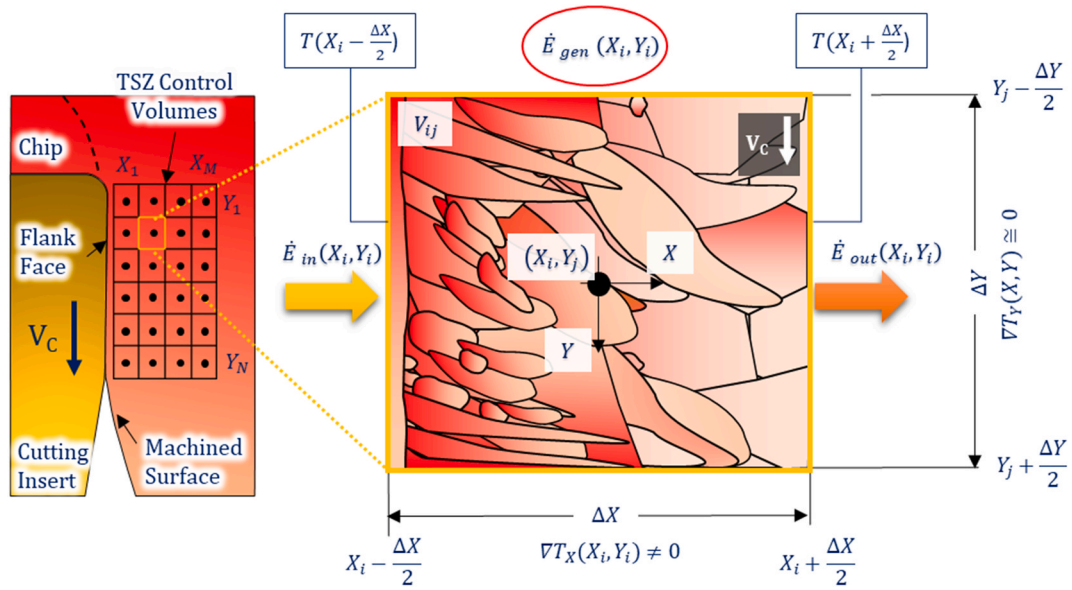


Fig. 17. Schematic representation of the grid of control volumes in TSZ where thermal balance equations are applied to evaluate the space-time distribution of heat generation in the machined workpiece subsurface.

As the thermal gradient in TSZ is parallel to X , the thermal energy leaving the control volume V_{ij} is equal to the heat flowing between its two boundaries at $X_i - \frac{\Delta X}{2}$ and $X_i + \frac{\Delta X}{2}$, as represented in Fig. 17. Indicating with k the workpiece thermal conductivity, Fourier's law for heat conduction allows calculation of $\dot{E}_{out}(X_i, Y_j)$ as:

$$\dot{E}_{out}(X_i, Y_j) = -k(T) \frac{\partial T(X_i, Y_j)}{\partial X} \quad (3)$$

Similarly, as the heat flux is regarded as one-dimensional and temperature decreases along X , the energy conducted in entrance in each control volume (X_i, Y_i) not in contact with the tool flank is equal to the amount of heat leaving the neighbouring volume at (X_{i-1}, Y_i) .

$$\dot{E}_{in}(X_i, Y_i) = \dot{E}_{out}(X_{i-1}, Y_i), \quad \forall V_{ij} | X_i > X_1 \quad (4)$$

On the other hand, for control volumes confining with the cutting insert, input heat can only be transferred from the adjacent tool's flank face. Hence, indicating this quantity as $\dot{E}_{out,flank}$, the thermal energy entering such volumes can be expressed as:

$$\dot{E}_{in}(X_i, Y_j) = \dot{E}_{out,flank}, \quad \forall V_{ij} | X_i = X_1 \quad (5)$$

The term $\dot{E}_{out,flank}$ in Eq. (5) could be evaluated from the flank-workpiece temperature difference through an estimation of the flank-workpiece thermal contact conductance h_C , which is not specifically available for the case of the flank-workpiece interaction within the aggressive pCBN cutting (Test #4) of the advanced Ni base superalloy under investigation. However, even by overestimating this value from available literature on tool-chip thermal conductance in SSZ [6], the heat exchange contribution with the tool flank in Eq. (5) is estimated to have a magnitude significantly lower than the terms in Eq. (3). Hence, in the following thermal balance analysis, the tool flank terms in Eq. (5) are neglected with respect to the internal heat conduction terms in Eq. (3).

Hence, Eqs. (1)–(5) allow to evaluate the heat transfer within the machined subsurface volume based on the thermal field measured in TSZ. In fact, TSZ temperature gradients exist as a consequence of the heat flow in the workpiece subsurface, where the plastic deformation process converts mechanical energy into thermal.

In this way, thermal energy balance in TSZ has been applied for the analysis of the temperature maps measured under aggressive cutting

with a pCBN insert ($V_C = 130$ m/min, $f = 0.15$ mm/rev, $r = 30$ μ m, $VB_0 = 0.2$ mm), as this can provide an interpretation on the formation mechanisms of material drag and nanocrystalline layers analysed in Section 4.2. Fig. 18a reports the measured thermal field for workpiece regions beyond the cutting insert, where the X -component of temperature gradients is plotted at increasing workpiece subsurface depths and at increasing Y -distances from the cutting edge.

More in detail, 14 Y -levels with ~ 20 μ m spacing have been selected to carry out thermal balance analysis at different times t after the cutting edge has been surpassed. As shown by the temperature profiles along Y_1 – Y_{14} in Fig. 18a, temperature fast decreases when moving perpendicularly to the machined surface, with a drop of ~ 350 $^{\circ}$ C moving at 60 μ m in the subsurface depth. On the other hand, much smaller temperature variations are found along Y , with temperatures being in a relatively narrow interval at each subsurface location X . Hence, this confirms the validity of Eq. (1) within the quasi-isothermal deformation zone with $\nabla T_Y \sim 0$. Thus, performing thermal balance analysis by means of Eqs. (2)–(4), the volumetric rate of heat generation due to plastic deformation in space and time has been obtained for the workpiece material passing through TSZ. The map in Fig. 19a represents the evolution of such heat generation developing in time and at different subsurface depths X as the workpiece advances and deforms in contact with the tool flank.

Highest values of heat generation within the TSZ plastic deformation process are found for $t \rightarrow 0$ and $X \rightarrow 0$, i.e. at the very start of the flank-workpiece contact and in correspondence of the material volumes closest to the machined surface. This indicates that the most severe plastic deformation develops at the beginning of the contact, where plasticity is concentrated within very thin layers adjacent to the workpiece surface. Shallow peaks in volumetric rates of heat generation approaching ~ 12 kW/mm³ are therefore associated with formation of nanocrystalline layers as the one in Fig. 19b. This correlates with the previous analysis that indicated how this process takes place at temperatures in the range of $\sim 10^3$ $^{\circ}$ C, and in material volumes having undergone heating rates in the range of 10^7 $^{\circ}$ C/s, which will subsequently cool down at $\sim 2 \times 10^6$ $^{\circ}$ C/s. At increasing times after the beginning of the contact, the rate of heat being generated decreases reaching values about a fourth of the peak (~ 3 kW/mm³) after ~ 0.1 ms, i.e. after a ~ 200 μ m travel beyond the cutting edge. This is associated with occurrence of strain hardening in the subsurface material volume, resulting in lower dislocation mobility and hence to increasing

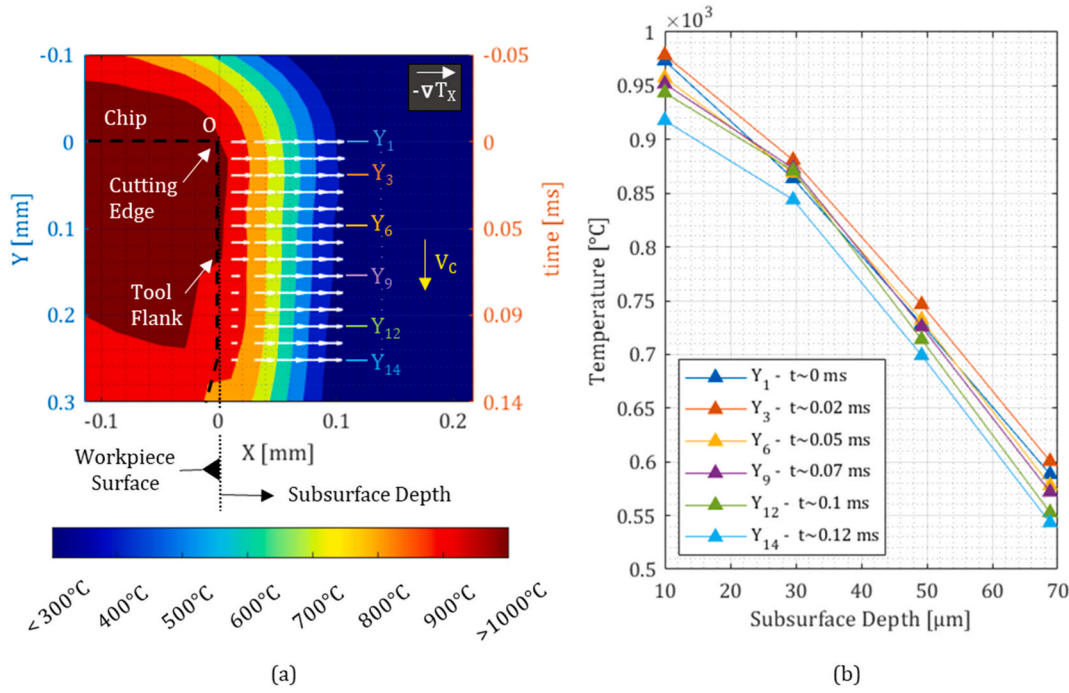


Fig. 18. Temperature profiles in tertiary shear zone perpendicularly to the machined surface. (a) Example of thermal map acquired at the flank-workpiece interface, with plot of X component of temperature gradients at increasing workpiece subsurface depths and for different Y-distances from the cutting edge. (b) Experimental temperature profiles beneath the workpiece subsurface at different distances from the cutting edge (X axis), i.e. at different times after entering in interaction with the tool's flank. Cutting experiment performed with a pCBN insert at $V_c = 130$ m/min, $f = 0.15$ mm/rev, $r = 30$ μm, $VB_0 = 0.2$ mm.

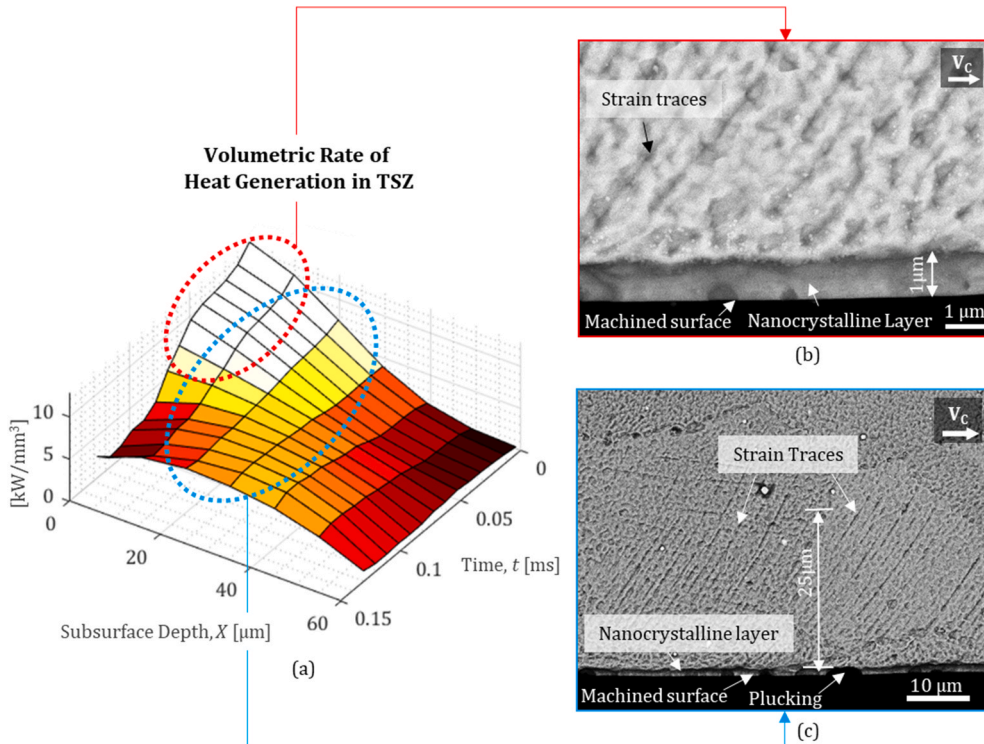


Fig. 19. Volumetric Rate of Heat Generation in TSZ in relation to microstructural deformation beneath workpiece subsurface. (a) Space-time distribution of heat generation below the machined surface at increasing times during its interaction with the tool flank. (b) Near-surface metallurgy with a 1-μm nanocrystalline layer and strained microstructure. (c) Machining-induced microstructural deformation with strain traces propagating below the machined surface over a depth of 25 μm. Cutting experiment performed with a pCBN insert at $V_c = 130$ m/min, $f = 0.15$ mm/rev, $r = 30$ μm, $VB_0 = 0.2$ mm.

resistance to further plastic deformation as the tool-workpiece interaction progresses. This can be linked to increased nano-hardness found in machining-induced white layers in nickel-base superalloys, e.g. as a result of broaching [33] or drilling [34].

A different trend is observed at higher depths in the workpiece subsurface. In fact, at the beginning of the flank-workpiece interaction

($t \rightarrow 0$), at subsurface depths $X \sim 20$ μm the rate of heat generation reaches significantly lower values (8 kW/mm^3) with respect to the very surface for $X \rightarrow 0$ ($\sim 12 \text{ kW/mm}^3$). Nevertheless, volumetric rates of heat generation are relatively high up to a distance $Y \sim 250$ μm ($t \sim 0.12$ ms) beyond the cutting edge, where they amount to $\sim 5 \text{ kW/mm}^3$ at subsurface depths $X \sim 30$ μm. Hence, although at intermediate subsurface

depths lower peaks are reached at the beginning of the contact, their decrease is slower over time. This indicates occurrence of less-severe plastic deformation developing over a longer time interval and more evenly spread over the workpiece-flank contact length, which has been associated with the formation of material drag layers as the one shown in Fig. 19c and to the less-severe subsurface plasticity observed by EBSD analysis in Fig. 13.

4.6. Discussion

As introduced in Section 1, the analysis of the link between thermal field and microstructural deformation within machining represents a topic of interest, which has however been explored mainly for the study of primary and secondary shear zones [19,35]. Temperature measurements were used to analyse thermal phenomena involving the workpiece volume [9,10], however with missing links to the resulting microstructural condition. Whilst state-of-the-art investigations are continuously advancing the existing understanding on the metallurgy of material drag and nanocrystalline layers [17,33] in machined surfaces, full comprehension of their formation mechanisms still requires an in-depth understanding of the physical conditions under which they are induced, i.e. as the newly cut surface interacts with the tool flank instants after its generation.

However, although the severity of cutting-induced thermal and mechanical effects can provide important insights on the phenomena developing at the tool-workpiece interface, it has been shown how they are unable to be generally associated to the deformation mechanism of machined surfaces. Therefore, a more comprehensive description of the thermal history of surface deformation has been implemented to account of the combined influence of thermal field severity and of the rates

at which the deformation process takes place in the workpiece subsurface. In this way, analysis of cutting-induced thermal cycles has not only enabled a quantitative description of the time-evolving thermal conditions induced in the machined surfaces during cutting, but also revealed how the severity of microstructural deformation could be qualitatively related to their magnitude and evolution.

Furthermore, application of thermal balance equations in TSZ has allowed the stages of heat generation in the workpiece subsurface due to its own plastic deformation to be discussed in relationship to the severity of microstructural condition observed by metallurgical analysis.

Thus, combining the information available from thermal cycle analysis and TSZ heat generation mapping, the microscale thermo-mechanical history of surface deformation can be described according to the process represented in Fig. 20, which comprises the following steps.

Step I: Even if they are not deformed into a chip, before entering TSZ, workpiece subsurface layers transit in close proximity to the tool-chip interface, where thermo-mechanical fields propagate from the nearby chip formation area. Hence, at the beginning of the interaction between the workpiece material and the tool's flank, TSZ entry boundary conditions see the inlet workpiece material in a pre-heated state. Heating rates magnitude strongly depends on the cutting process thermo-physical boundary conditions (insert material, speed, feed, etc.) with values in the range of 10^6 °C/s and 10^7 °C/s under conventional and aggressive cutting conditions, respectively. Peaks in thermal gradients have been found to relate with the severity of microstructural deformation, as the heat flux enabling these gradients to exist is provided by heat generation due to plastic deformation. However, their space distribution does not directly correspond to the locations where plasticity occurs, as local heat transfer conditions allowed high gradients

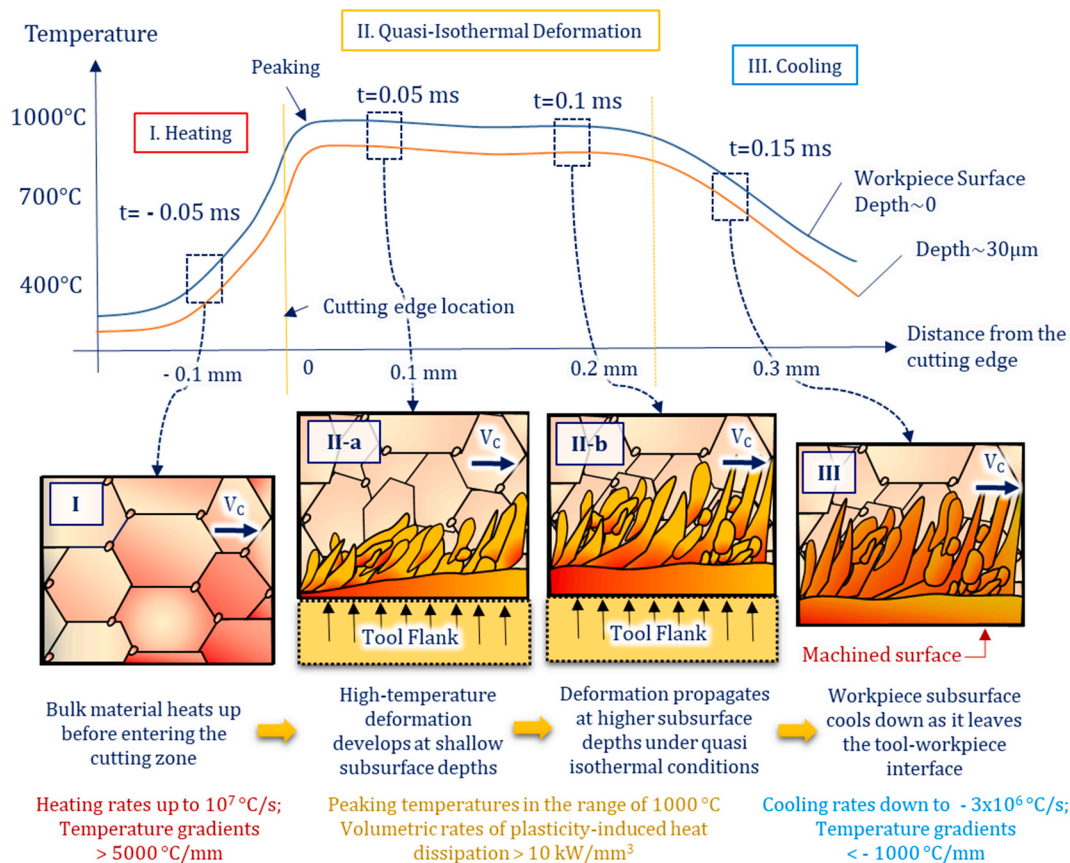


Fig. 20. Schematic of the thermal history of microstructural surface deformation induced at the tool-workpiece interface. Different microstructural conditions are conceptually represented corresponding to each step of the machining-induced thermo-mechanical cycle within the workpiece subsurface volume (with reference to the present case study involving cutting of an advanced Nickel-base superalloy).

to propagate at deep subsurface levels where no traces of deformation was found.

Step II: Hot metal mechanically engages with the tool flank, where the dynamic contact pressure induces high-temperature subsurface shear. As a result, microstructural subsurface deformation develops, sweeping grain boundaries and inducing high lattice distortion to the adjacent workpiece layers. Temperature peaks are hence reached shortly beyond the cutting edge, with the extension of the temperature peaking zone widening as the intensity of the thermomechanical interaction increases, inducing a distinct quasi-isothermal deformation region under the most aggressive cutting scenarios. As under such conditions isothermal lines become parallel to the flank-workpiece relative motion, energy balance performed perpendicularly to the cut surface has allowed the distribution of heat generation to be evaluated in TSZ. Thus, analysis of the volumetric rate of heat generation in the workpiece subsurface revealed that most severe plasticity is to be expected in thin surface layers and at the beginning of the flank-workpiece contact. This has been associated to generation of the nanocrystalline (white) layers previously identified by analysis of microstructural surface integrity. Subsequently, heat generation fast decreases at shallow subsurface depths before leaving the flank contact region, which is attributed to a fast decreasing dislocation mobility within such highly distorted surface layers offering increasing resistance to further strain. Hence, surface loads resulting from the ongoing tool-workpiece interaction are transmitted at higher depths into the workpiece. In fact, although in these regions heat generation induced by plastic deformation was lower than at the surface at the beginning of the contact, its magnitude keeps a more constant trend when shallow depths heat generation decreases. This has hence indicated that at increasing subsurface depths, a less severe and more evenly spread plastic deformation process takes place, which has been associated with formation of material drag layers previously observed by metallurgical surface inspection.

Step III: Finally, a cooling phase takes place as the strained subsurface volumes move away from the flank contact region. Even though the cooling phase is found to occur at rates significantly slower than the ones encountered in the heating phase, subsurface cooling is still extremely fast in absolute values with temperature decreasing at rates down to -3×10^6 °C/s at the highest surface speeds tested within this research. As this cooling phase has been accounted for gamma prime phase suppression and growth of recrystallized grains in white layers generated when mechanically machining advanced Ni-base superalloys [17], investigating and quantifying the nature of the ultra-fast cooling imposed to the previously deformed surface layers has primary importance to understand the resulting surface metallurgy.

5. Conclusions

Revealing the nature of the thermo-mechanical conditions induced by cutting processes plays a pivotal role to understand the mechanisms controlling the metallurgical integrity of machined surfaces. To this aim, the present research has investigated the thermal history of machining-induced microstructural surface deformation under different combinations of thermal and mechanical effects, for a case study considering the cutting of a next-generation Ni-base superalloy. Thus, this has allowed the following points to be addressed:

1. For the first time, thermal cycles induced in the machined surfaces while crossing the tool-workpiece interface have been described and linked to the resulting microstructural surface integrity. A Heating-Peaking-Cooling (H-P-C) thermal cycle has been identified under thermo-mechanical conditions of intermediate severity generated by different combinations of thermal and mechanical effects, which induced heating and cooling rates in the range of $\sim 3 \times 10^6$ °C/s and $\sim 10^6$ °C/s to the workpiece subsurface. In this way, it has been discussed how the different combinations of mechanical ($f = 0.1$ mm/rev, $r = 7$ μ m, $VB_0 = 0$ mm, $V_C = 30$ m/min for CC and 70 m/min for

pCBN inserts) and thermal effects (tool tip temperatures in the order of ~ 900 °C for CC and ~ 700 °C for pCBN inserts) can result in comparable thermal cycles, with their shape and magnitude relating with the severity of cutting-induced microstructural deformation (11–15 μ m material drag layers). Thus, analysis of the thermal history was not only able to describe the exceptional conditions under which metallurgical anomalies were generated, but it could as well provide an indication on the extent of the cutting-induced subsurface deformation.

2. Microscale deformation at each subsurface depth was found to occur under almost constant temperature along the tool-workpiece flank contact region under high-intensity thermo-mechanical effects. In fact, under increased flank-workpiece mechanical engagement (due to flank wear and a rounded cutting edge) a high-temperature quasi-isothermal deformation region has been observed in tertiary shear, as shown by the case study presented under aggressive processing conditions (tool tip temperatures up to ~ 1100 °C, $V_C = 130$ m/min, $f = 0.15$ mm/rev, $r = 30$ μ m, $VB_0 = 0.2$ mm). Specifically, subsurface thermal cycles under severe thermo-mechanical effects have been identified as a sequence of Heating, Quasi-Isothermal Deformation and Cooling (H-Q-C), with extreme heating and cooling rates approaching values of $\sim 10^7$ °C/s and $\sim 3 \times 10^6$ °C/s, respectively, which are associated to the formation of ~ 1 μ m-deep nanocrystalline layers and ~ 24 μ m material drag layers. In this way, this has further highlighted the existing link between the severity of thermal cycles and the resulting surface metallurgy.
3. The thermo-mechanical stages of material drag and nanocrystalline layers formation have been revealed by analysis of the rates of heat generation in the workpiece subsurface as a result of plastic deformation in tertiary shear zone. Thus, the plastic deformation mechanism of workpiece layers mechanically interacting with the tool flank has been revealed by application of energy balance equations over a mesh of TSZ control volumes, for a case study considering the high-temperature deformation of an advanced Nickel-base superalloy. This has allowed the different stages of plasticity to be uncovered, with volumetric rates of heat generation approaching ~ 12 kW/mm³ at the beginning of the contact and within volumes nearest to the workpiece surface.
4. Finally, a comprehensive and general analysis associating heating-cooling rates and heat generation to both the thermo-mechanical boundary conditions and to the resulting microstructural surface integrity was outlined. This has provided an informed description of the process transforming bulk material regions into highly strained material layers, with particular references on the extreme physical conditions developing when mechanically machining next generation nickel-base superalloys.

In this way, the present research has systematically investigated the thermal field evolution characterising the microstructural surface deformation process induced by mechanical material removal, and its link to the resulting metallurgical surface integrity. In particular, the knowledge developed in this work has been applied to study the case of an advanced Ni-base superalloy for high-temperature applications, providing unprecedented knowledge on the physical conditions under which machining-induced layers are generated in this unique class of materials. In addition, further research on the relationship between thermal fields in TSZ and surface deformation could enable the development of advanced process optimisation approaches or even in-situ surface integrity estimation through monitoring of temperature evolution in the machined surface volume. Furthermore, it is believed that the knowledge presented in this work is not only limited to mechanical machining processes, but can be translated for a wider understanding of manufacturing processes where severe plastic deformation is induced, by means of an energy-based description of the thermo-mechanical conditions induced to metals in relationship to the resulting metallurgical state.

Credit author statement

Andrea la Monaca: Investigation, Methodology, Formal analysis, Conceptualization, Visualization, Data Curation, Writing - original draft, Writing - review & editing. **Dragos Axinte:** Methodology, Formal analysis, Conceptualization, Visualization, Supervision, Writing - review & editing. **Zhirong Liao:** Formal analysis, Resources, Supervision, Writing - review & editing. **Rachid M'Saoubi:** Methodology, Formal analysis, Conceptualization, Resources, Supervision, Writing - review & editing. **Mark Hardy:** Methodology, Formal analysis, Conceptualization, Resources, Supervision, Writing - review & editing.

Declaration of competing interest

The authors declare that they have no known competing financial interests or personal relationships that could have appeared to influence the work reported in this paper.

Acknowledgment

The authors would like to acknowledge Rolls-Royce plc and Seco Tools AB for permission to publish this work and provision of financial support. Rolls-Royce plc is further acknowledged for provision of workpiece material, while Seco Tools AB is acknowledged for allowing the cutting tests to be carried out at their facilities. The authors are especially grateful to Mr Per Alm from Seco Tools AB for his support within the thermal imaging of the metal cutting experiments. This study was further supported by EPSRC through the NanoPrime initiative (EPSRC Reference: EP/R025282/1). The Nanoscale and Microscale Research Centre (nmRC) at the University of Nottingham is also acknowledged for providing access to their facilities.

References

- Z. Liao, A. la Monaca, J. Murray, A. Speidel, D. Ushmaev, A. Clare, D. Axinte, R. M'Saoubi, Surface integrity in metal machining - Part I: fundamentals of surface characteristics and formation mechanisms, *Int. J. Mach. Tool Manufact.* 162 (2021) 103687, <https://doi.org/10.1016/j.ijmactools.2020.103687>.
- A. la Monaca, J.W. Murray, Z. Liao, A. Speidel, J.A. Robles-Linares, D.A. Axinte, M. C. Hardy, A.T. Clare, Surface integrity in metal machining - Part II: functional performance, *Int. J. Mach. Tool Manufact.* (2021) 103718, <https://doi.org/10.1016/j.ijmactools.2021.103718>.
- N.A. Abukhshim, P.T. Mativenga, M.A. Sheikh, Heat generation and temperature prediction in metal cutting: a review and implications for high speed machining, *Int. J. Mach. Tool Manufact.* (2006), <https://doi.org/10.1016/j.ijmactools.2005.07.024>.
- G. Hao, Z. Liu, Experimental study on the formation of TCR and thermal behavior of hard machining using TiAlN coated tools, *Int. J. Heat Mass Transf.* 140 (2019) 1–11, <https://doi.org/10.1016/j.ijheatmasstransfer.2019.05.108>.
- V. Kryzhanivskyy, V. Bushlya, O. Gutnichenko, R. M'Saoubi, J.E. Ståhl, Heat flux in metal cutting: experiment, model, and comparative analysis, *Int. J. Mach. Tool Manufact.* 134 (2018) 81–97, <https://doi.org/10.1016/j.ijmactools.2018.07.002>.
- V. Kryzhanivskyy, R.M. Saoubi, J.E. Ståhl, V. Bushlya, Tool-chip thermal conductance coefficient and heat flux in machining: theory, model and experiment, *Int. J. Mach. Tool Manufact.* 147 (2019) 103468, <https://doi.org/10.1016/j.ijmactools.2019.103468>.
- A.W. Nemetz, W. Daves, T. Klünsner, W. Ecker, J. Schäfer, C. Czettel, T. Antretter, Cyclic heat-up and damage-relevant substrate plastification of single- and bilayer coated milling inserts evaluated numerically, *Surf. Coating Technol.* 360 (2019) 39–49, <https://doi.org/10.1016/j.surfcoat.2019.01.008>.
- K. Huang, W. Yang, Analytical model of temperature field in workpiece machined surface layer in orthogonal cutting, *J. Mater. Process. Technol.* 229 (2016) 375–389, <https://doi.org/10.1016/j.jmatprotec.2015.07.008>.
- L. Chen, B.L. Tai, R.G. Chaudhari, X. Song, A.J. Shih, Machined surface temperature in hard turning, *Int. J. Mach. Tool Manufact.* 121 (2017) 10–21, <https://doi.org/10.1016/j.ijmactools.2017.03.003>.
- M. Cuesta, P. Aristimuño, A. Garay, P.J. Arrazola, Heat transferred to the workpiece based on temperature measurements by IR technique in dry and lubricated drilling of Inconel 718, *Appl. Therm. Eng.* 104 (2016) 309–318, <https://doi.org/10.1016/j.applthermaleng.2016.05.040>.
- A. la Monaca, Z. Liao, D. Axinte, A digital approach to automatically assess the machining-induced microstructural surface integrity, *J. Mater. Process. Technol.* 282 (2020) 116703, <https://doi.org/10.1016/j.jmatprotec.2020.116703>.
- R. M'Saoubi, D. Axinte, C. Herbert, M. Hardy, P. Salmon, Surface integrity of nickel-based alloys subjected to severe plastic deformation by abusive drilling, *CIRP Ann. - Manuf. Technol.* 63 (2014) 61–64, <https://doi.org/10.1016/j.cirp.2014.03.067>.
- S.B. Hosseini, U. Klement, Y. Yao, K. Rytberg, Formation mechanisms of white layers induced by hard turning of AISI 52100 steel, *Acta Mater.* 89 (2015) 258–267, <https://doi.org/10.1016/j.actamat.2015.01.075>.
- D. Xu, Z. Liao, D. Axinte, M. Hardy, A novel method to continuously map the surface integrity and cutting mechanism transition in various cutting conditions, *Int. J. Mach. Tool Manufact.* 151 (2020) 103529, <https://doi.org/10.1016/j.ijmactools.2020.103529>.
- M. Brown, P. Crawforth, R. M'Saoubi, T. Larsson, B. Wynne, A. Mantle, H. Ghadbeigi, Quantitative characterization of machining-induced white layers in Ti–6Al–4V, *Mater. Sci. Eng. A* 764 (2019) 138220, <https://doi.org/10.1016/j.msea.2019.138220>.
- R. M'Saoubi, T. Larsson, J. Outeiro, Y. Guo, S. Suslov, C. Saldana, S. Chandrasekar, Surface integrity analysis of machined Inconel 718 over multiple length scales, *CIRP Ann. - Manuf. Technol.* 61 (2012) 99–102, <https://doi.org/10.1016/j.cirp.2012.03.058>.
- Z. Liao, M. Polyakov, O.G. Diaz, D. Axinte, G. Mohanty, X. Maeder, J. Michler, M. Hardy, Grain refinement mechanism of nickel-based superalloy by severe plastic deformation - mechanical machining case, *Acta Mater.* 180 (2019) 2–14, <https://doi.org/10.1016/j.actamat.2019.08.059>.
- C. Huang, T.G. Murthy, M.R. Shankar, R. M'Saoubi, S. Chandrasekar, Temperature rise in severe plastic deformation of titanium at small strain-rates, *Scripta Mater.* 58 (2008) 663–666, <https://doi.org/10.1016/j.scriptamat.2007.11.042>.
- B. Medina-Clavijo, M. Saez-de-Buruaga, C. Motz, D. Soler, A. Chuvilín, P. J. Arrazola, Microstructural aspects of the transition between two regimes in orthogonal cutting of AISI 1045 steel, *J. Mater. Process. Technol.* 260 (2018) 87–96, <https://doi.org/10.1016/j.jmatprotec.2018.05.016>.
- Z. Liao, D. Axinte, M. Mieszala, R. M'Saoubi, J. Michler, M. Hardy, On the influence of gamma prime upon machining of advanced nickel based superalloy, *CIRP Ann* 67 (2018) 109–112, <https://doi.org/10.1016/j.cirp.2018.03.021>.
- J. Plummer, Understanding a way to fly high, *Nat. Mater.* 15 (2016) 819–820, <https://doi.org/10.1038/nmat4699>.
- M.C. Hardy, M. Detrois, E.T. McDevitt, C. Argyrakis, V. Saraf, P.D. Jablonski, J. A. Hawk, R.C. Buckingham, H.S. Kitaguchi, S. Tin, Solving recent challenges for wrought Ni-base superalloys, *Metall. Mater. Trans. A* (2020), <https://doi.org/10.1007/s11661-020-05773-6>.
- M.C. Hardy, B. Zirbel, G. Shen, R. Shenkar, Developing damage tolerance and creep resistance in a high strength nickel alloy for disc applications, in: *Superalloys 2004* (Tenth Int. Symp., TMS, 2004, pp. 83–90, https://doi.org/10.7449/2004/Superalloys_2004_83_90.
- K.A. Christofidou, M.C. Hardy, H.Y. Li, C. Argyrakis, H. Kitaguchi, N.G. Jones, P. M. Mignaneli, A.S. Wilson, O.M.D.M. Messé, E.J. Pickering, R.J. Gilbert, C.M. F. Rae, S. Yu, A. Evans, D. Child, P. Bowen, H.J. Stone, On the effect of Nb on the microstructure and properties of next generation polycrystalline powder metallurgy Ni-based superalloys, *Metall. Mater. Trans. A Phys. Metall. Mater. Sci.* 49 (2018) 3896–3907, <https://doi.org/10.1007/s11661-018-4682-4>.
- R.C. Buckingham, C. Argyrakis, M.C. Hardy, S. Biroscu, The effect of strain distribution on microstructural developments during forging in a newly developed nickel base superalloy, *Mater. Sci. Eng. A* 654 (2016) 317–328, <https://doi.org/10.1016/j.msea.2015.12.042>.
- R. M'Saoubi, D. Axinte, S.L. Soo, C. Nobel, H. Attia, G. Kappmeyer, S. Engin, W. M. Sim, High performance cutting of advanced aerospace alloys and composite materials, *CIRP Ann. - Manuf. Technol.* 64 (2015) 557–580, <https://doi.org/10.1016/j.cirp.2015.05.002>.
- D. Soler, T.H.C. Childs, P.J. Arrazola, A note on interpreting tool temperature measurements from thermography, *Mach. Sci. Technol.* 19 (2015) 174–181, <https://doi.org/10.1080/10910344.2014.991027>.
- P.-J. Arrazola, P. Aristimuño, D. Soler, T. Childs, Metal cutting experiments and modelling for improved determination of chip/tool contact temperature by infrared thermography, *CIRP Ann* 64 (2015) 57–60, <https://doi.org/10.1016/j.cirp.2015.04.061>.
- E. Ezugwu, J. Bonney, Y. Yamane, An overview of the machinability of aeroengine alloys, *J. Mater. Process. Technol.* 134 (2003) 233–253, [https://doi.org/10.1016/S0924-0136\(02\)01042-7](https://doi.org/10.1016/S0924-0136(02)01042-7).
- M.C. Hardy, R.C. Reed, D. Crudden, Nickel-base Superalloy, United States Patent US10422024B2, 2019.
- A. Bhatt, H. Attia, R. Vargas, V. Thomson, Wear mechanisms of WC coated and uncoated tools in finish turning of Inconel 718, *Tribol. Int.* 43 (2010) 1113–1121, <https://doi.org/10.1016/j.triboint.2009.12.053>.
- C.R.J. Herbert, J. Kwong, M.C. Kong, D.A. Axinte, M.C. Hardy, P.J. Withers, An evaluation of the evolution of workpiece surface integrity in hole making operations for a nickel-based superalloy, *J. Mater. Process. Technol.* 212 (2012) 1723–1730, <https://doi.org/10.1016/j.jmatprotec.2012.03.014>.
- Z. Chen, M.H. Colliander, G. Sundell, R.L. Peng, J. Zhou, S. Johansson, J. Moverare, Nano-scale characterization of white layer in broached Inconel 718, *Mater. Sci. Eng. A* 684 (2017) 373–384, <https://doi.org/10.1016/j.msea.2016.12.045>.
- C.R.J. Herbert, D.A. Axinte, M.C. Hardy, P.D. Brown, Investigation into the characteristics of white layers produced in a nickel-based superalloy from drilling operations, *Procedia Eng* 19 (2011) 138–143, <https://doi.org/10.1016/j.proeng.2011.11.092>.
- M.R. Shankar, B.C. Rao, S. Lee, S. Chandrasekar, A.H. King, W.D. Compton, Severe plastic deformation (SPD) of titanium at near-ambient temperature, *Acta Mater.* 54 (2006) 3691–3700.